Pallium-encoded valence-specific chemosensory amplification of eye-body coordination in larval zebrafish

Samuel K. H. Sy,[1-7,*] Danny C. W. Chan,[1-5] Jenny J. Zhang,[1-5] Jing Lyu,[1-5] Crystal Feng,[1-5] Kui Wang,[8] Vincent C. T. Mok,[1-5] Kenneth K. Y. Wong,[6,9] Yu Mu,[8] Yu Hu,[10] Ho Ko[1-5,*]

Affiliations

[1]Division of Neurology, Department of Medicine and Therapeutics, Faculty of Medicine, The Chinese University of Hong Kong, Shatin, New Territories, Hong Kong SAR, China.

[2]Li Ka Shing Institute of Health Sciences, Faculty of Medicine, The Chinese University of Hong Kong, Shatin, New Territories, Hong Kong SAR, China.

[3]Margaret K. L. Cheung Research Centre for Management of Parkinsonism, Faculty of Medicine, The Chinese University of Hong Kong, Shatin, New Territories, Hong Kong SAR, China.

[4]Lau Tat-chuen Research Centre of Brain Degenerative Diseases in Chinese, Faculty of Medicine, The Chinese University of Hong Kong, Shatin, New Territories, Hong Kong SAR, China.

[5]Gerald Choa Neuroscience Institute, The Chinese University of Hong Kong, Shatin, New Territories, Hong Kong SAR, China.

[6]Advanced Biomedical Instrumentation Centre, Hong Kong Science Park, Pak Shek Kok, New Territories, Hong Kong SAR, China.

[7]Department of Biology and Psychology, University of Göttingen, Göttingen, Germany.

[8]Institute of Neuroscience, Chinese Academy of Sciences, Shanghai, China.

[9]Department of Electrical and Electronic Engineering, Faculty of Engineering, The University of Hong Kong, Pok Fu Lam, Hong Kong Island, Hong Kong SAR, China.

[10]Department of Mathematics and Division of Life Science, School of Science, Hong Kong University of Science and Technology, Clear Water Bay, New Territories, Hong Kong SAR, China.

[*]Correspondence: S.K.H.S. (khsamuelsy@gmail.com) or H.K. (ho.ko@cuhk.edu.hk)

Summary

Coordinated eye-body movements are essential for adaptive behavior, yet little is known about how multisensory input, particularly chemosensory cues, shapes this coordination. Using our enhanced Fish-On-Chips optofluidic platform, we uncovered complex dynamics in how larval zebrafish coordinate saccadic eye movements with tail flips. Under baseline conditions, spontaneous tail flips dynamically align with saccades in frequency and direction for coordinated turns. Chemosensory valence further modulates this coordination: death-associated cues intensify both the strength and frequency of coupled saccade-tail flips during turns, whereas food-related cues promote forward gliding without altering saccade coupling. Concurrent brain-wide neuronal imaging reveals that the zebrafish pallium represents the transformation of aversive valence into enhanced saccade-tail coordination, with stronger coupling associated with higher pallium activation. These findings uncover the neural basis by which chemosensory inputs of different valences distinctly regulate eye-body coordination to drive adaptive locomotion in a developing vertebrate, offering insights into principles of sensory-motor integration.

Introduction

Eye-body coordination underpins a wide range of visuomotor behaviors across the animal kingdom, enabling animals to adapt to their environments and perform critical tasks such as hunting, navigation and foraging [1–3]. In many vertebrates, quick and synchronous movements of both eyes in the same direction, known as conjugate saccades (hereafter referred to as saccades), play a key role in aligning gaze with body orientation, facilitating precise tracking of moving objects and stable navigation through complex environments [4–8]. Disruption to this coordination, such as in Parkinson's disease, is linked to motor impairments like turning difficulties [9]. Such eye-body coordination is well-illustrated in *Xenopus laevis* larvae, where compensatory eye movements during locomotion are driven by feedforward efference copies of spinal central pattern generator activity [10]. Similar mechanisms have also been observed in mice [11]. These signals synchronize eye movements with spinal and tail undulations to stabilize gaze during swimming while overriding reactive sensory feedback such as vestibulo-ocular reflexes [10,12]. Although visual and mechanosensory cues are traditionally thought to dominate visuomotor control [13–20], an animal often needs to integrate information from multisensory modalities to optimize decision making and motor program selection [21–25].

Chemosensation, one of the most ancient sensory systems [26], plays a pivotal role in locomotion by modulating heading direction in response to chemical cues with innate and/or learnt valence values [27–40]. These cues provide critical information about the environment, which can signal the presence of food [28] or predators [29,30], driving context-specific motor responses like fleeing or orienting. For example, a sudden surge of noxious chemical signals can trigger fleeing. While chemosensory valence is well-known to shape body movements, its influence on eye movements and eye-body coordination remains poorly understood. In addition, chemical cues may trigger arousal state changes, leading to more frequent visual scanning and heightened alertness [41]. Understanding how chemosensory cues interact with visuomotor behaviors could provide key insights into the mechanism of multisensory integration and motor control.

In this study, we investigated how chemosensory valence modulates the coordination of eye and body movements in larval zebrafish. Zebrafish are an ideal model for studying sensorimotor integration due to their lack of a flexible neck (i.e., the anatomy limits independent yaw (side-to-side) movement of the head), which simplifies kinematic analysis [42,43]. Their optical transparency also allows for brain-wide neuronal imaging, making them highly suitable for studies of neural circuit activity [44]. We hypothesized that chemosensory cues trigger a coordinated behavioral response in larval zebrafish with saccades and tail flips jointly modulated by cue valence. To test this, we advanced our Fish-on-Chips system [27], enabling simultaneous behavioral analysis and brain-wide imaging and efficient chemical valence screening in freely responding larvae. This approach allowed us to elucidate the neural mechanisms by which chemosensory input regulates coordinated visuomotor behaviors.

We revealed that temporally coupled saccade-body turns are characterized by a larger turn intent, and exhibit dynamic directional alignment and temporal coordination. In contrast, these characteristics are not observed in saccade-independent forward swims. Upon exposure to chemosensory stimuli, coupled saccade-turn is enhanced by aversive death-associated but not appetitive food-related chemicals. Across the brain, we identified neuronal signatures underlying chemosensory input-amplified coupled saccade-tail flips, pinpointing the telencephalic pallium as a potential key coordinator. Our findings indicate that in larval zebrafish, chemosensory cues can influence eye-body coordination based on innate perceived valence, serving as an integrated response to achieve locomotive goals.

Results

Fish-on-Chips 2.0 enables efficient valence screening and naturalistic behavior-neural imaging under chemical cue delivery

Despite tremendous efforts in developing appropriate methodology for the study of chemosensation in small animals, previous methods [45–48], including our own [27], have fallen short of achieving high-throughput, spatiotemporally precise valence screening and naturalistic behavioral readout under repeated delivery of multiple chemical cues—a challenge that we address in our study. To address this gap, we advance our Fish-on-Chips platform to demonstrate significantly improved experimental conditions for the mechanistics studies of behavioral and neural effects of chemicals on larval zebrafish.

First, we developed an improved valence assay (see **Methods, Figures 1a, b, Supplementary Figure 1a**) that allowed us to efficiently screen preferences of ecologically significant chemicals or odors across multiple orders of concentrations using the same animals, covering wide dynamic ranges of chemoreception in teleosts [49]. These included two amino acids, namely valine (Val) and alanine (Ala) [32,33], the sex pheromone prostaglandin F2α (PGF2α) [31], putrefaction-associated diamines including cadaverine (Cad) and putrescine (Put) [27,29], bile acids [35,36] including chenodeoxycholic acid (CDCA) and glycodeoxycholic acid (GDCA), adenosine (Ade) which is a food-associated cue [28], and sodium chloride (NaCl) which determines salinity [34].

In control conditions with all quadrants filled with water, the larval zebrafish distribute their time evenly across the four quadrants, indicating no intrinsic bias in the setup (**Figure 1c**).

We observed that Val (at 100 μM or above) and Ala (at 10 μM and 1 mM) are attractive to the larvae, similar to the preference seen in adult zebrafish [32,33]. Interestingly, despite being a sex pheromone [31], PGF2α is already attractive to the larval zebrafish at a concentration of 1 μM. We also confirmed that Cad and Put, at 10 μM or 100 μM and above, respectively, are repellent [27,29]. CDCA (at 10 μM and above) and GDCA (at 1 μM and above), which are examples of bile acids typically considered as social cues at low concentrations [35,36], were found to be repellant. For PGF2α and the bile acids, which require 0.5% DMSO for dissolution, we obtained consistent results comparing data using either water or 0.5% DMSO in the control quadrant (**Supplementary Figures 1b, c**), and therefore pooled the results for analysis (**Figure 1c**).

Notably, larval zebrafish generally respond to attractive and aversive chemicals at the highest concentration tested, with the exception of PGF2α. Adenosine, known to attract adult zebrafish [28], did not exhibit any attractant or repellent effects on the larvae. Furthermore, NaCl, a recently reported aversive olfactory stimulus [34], showed no impacts on the larvae in our assays. Note that however, our assay predominantly presents absolute concentrations of NaCl with minimal gradient, which could be a critical factor as zebrafish may rely on its spatial gradient for navigation to avoid high salinity areas [34].

Next, in our new imaging setup for enhanced larva tethering, chemical delivery and brainwide neuronal imaging abilities (see **Methods, Figure 1d, Supplementary Figure 2**), we observed robust spontaneous saccades and tail flips (during blank trials and pre-stimulus windows) across five larval subjects (**Figure 1e, Supplementary Figure 2b**), with tail flip frequency comparable to that of freely moving larvae [50]. Notably, spontaneous saccades occurred less frequently than spontaneous tail flips, as indicated by the longer median pre-event interval (PEI, defined as difference in onset times between an event and the preceding one) for saccades (5.63 seconds; n = 216 saccades from 5 larvae) vs. tail flips (0.90 seconds; n = 1,018 tail flips from 5 larvae). Since these behaviors preserve more naturalistic behavior (in terms of saccade and tail flip frequencies) compared to that reported with the conventional agarose-based tethering approaches (**Figure 1e**), the setup is well-posed for the study of both the behavioral and neural effects under highly controlled chemical stimulus delivery.

Tail flip dynamically aligns with saccade in rate and direction for spontaneous turns

As mentioned, numerous studies have shown that eye and body movements are precisely coordinated during single spontaneous orientation changes in larval zebrafish [6,7] and other vertebrates. However, it remains unclear how saccades and tail flips—two quasi-periodic movements that occur at vastly different rates (**Figure 1e, Supplementary Figure 2b**)—are coordinated during self-initiated turns. Interestingly, this coordination contrasts with predictions of smooth and pre-planned movements in some motor control models [51,52]. We hypothesize that this coordination extends beyond individual events and requires the dynamic spatiotemporal matching of the more frequently occurring tail flips to saccades. To test this, we analyzed the recorded baseline behaviors.

We first isolated the co-occurrences of saccades and tail flips, defining temporally coupled saccade-tail flip events (hereafter referred to as S-T events) as those with saccade and tail flip onset time difference of 0.5 seconds or less. This threshold is based on it being approximately half the median PEI of the more frequent tail flips. Other non-coupled saccade

or tail flip events are referred to as independent events. We first examined the relative timings of saccade and tail flip in an S-T event (**Figure 2a**). The tail flip typically occurred after the coupled saccade (**Figure 2b**), with their durations largely overlapping (**Supplementary Figure 3a**), and much shorter latency in offsets compared with onsets (**Figure 2c, Supplementary Figure 3b**), indicating that they represent coordinated eye-body movements at individually event levels. Overall, 52.1% of saccades and 15.4% of tail flips occurred in S-T events (**Supplementary Figure 3c**). Beyond single events, there is evident temporal coordination in their rate compared with when saccades and tail flips occur independently, for which these intervals remained relatively stable (**Figures 2d, e**). Following an S-T event, the PEI for the subsequent saccade increased by about 20% (**Figure 2d**), effectively extending the time for gaze fixation. For tail flips, their PEI around S-T events significantly lengthened, more than doubling in magnitude from 6 prior tail flips to the peak at S-T events, then decreasing back to the baseline over a few tail flips (**Figure 2e**). This pattern indicates that temporal control in S-T events is based on anticipatory and dynamic regulation extending beyond individual occurrence, similar to many other timed behaviors [53].

During single S-T events, saccades and tail flips are predominantly ipsilateral (i.e., towards the same body side) (**Figure 2f**), in line with previous reports [6,7]. Considering the dynamic nature of saccade-tail flip coordination, we investigated the directional synchronization of these movements, by analyzing the directionality of both movements in independent and coordinated events. Consecutive saccades mostly alternated in direction (**Supplementary Figure 3d**), and such a pattern did not differ between independent saccades vs. those of S-T events (**Figure 2g**). In contrast, tail flips generally exhibited an ipsilateral tendency relative to each preceding flip (**Supplementary Figure 3e**) and maintained this pattern across a series of tail flips (**Figure 2h, *teal curve***). This aligns with previous findings that the directionality of tail flip is dependent on history [54]. Interestingly, when aligned to S-T events, the dominant direction of tail flip gradually alternated from and to the contralateral side over ±5–6 tails flips (**Figure 2h, *coral curve***). As the median pre-saccade interval was also around 6 times that of pre-tail flip interval (**Figure 1e**), this gradual modulation likely permits directional alignment of tail flips with consecutive saccades.

We further analyzed the relationship between S-T events and putative locomotive intent using kinematic parameters of each tail flip extracted from time-series tail angle data (**Supplementary Figure 3f**). The pre-tail flip interval is associated positively with the magnitude and tail flip asymmetry (**Supplementary Figures 3g–i**), and negatively with the average undulation (**Supplementary Figure 3j**), of tail flips. Tail flip asymmetry gradually increased before and peaked at S-T events, followed by a decrease over a few tail flips (**Figure 2i, Supplementary Figure 3k**). This pattern appeared to recur approximately every 6–7 tail flips (**Figure 2i, Supplementary Figure 3k**). Changes in the average undulation exhibited an antiphasic pattern to that of tail flip asymmetry, peaking at around ±3rd tail flips relative to S-T events (**Figure 2j, Supplementary Figure 3l**). Together, these indicated that S-T events are associated with a greater orientation towards turning (see also similar/related findings in [6,7]) rather than sustained forward gliding [55], with the kinematics of tail flips modulated in an anticipatory manner along with S-T event timing.

Collectively, we concluded that in larval zebrafish, spontaneous coupled eye-tail flip movements involve highly organized motor coordination. This coordination, occurring through a sequence of tail events, is characterized by simultaneous occurrence of temporal synchronization, directional alignment, and kinematic modulation (**Figure 2k**), putatively for mediating body turns during locomotion.

Apart from saccade-coupling, the above-mentioned findings implicated that spontaneous swim bouts are dynamically organized around turns. Using the swim bout data alone from our previous study [27], we first verified the relationship between pre-bout interval and turn magnitude in larvae freely swimming in water (**Figure 3a**). We then classified the swim bouts into non-turn and turn bouts (see **Methods**), as surrogates for independent and saccade-coupled tail flips, respectively (recall that saccade-coupled tail flips have larger turning intent, **Figure 2i**). Upon comparative analysis, we found similar temporal (**Figure 3b**), directional (**Figures 3c, d**) and kinematic (**Figure 3e**) coordinations for the turn bouts, but not the non-turn bouts (**Figures 3b–e**). The behavioral manifestations of larval zebrafish in a freely moving arena therefore further substantiated that observed in the microfluidic device.

Chemical valence differentially modulates saccade-tail flip coordination

We next aimed to test whether chemical stimuli, often encountered unexpectedly in the natural environment, may influence eye movements and saccade-turn coordination. In response to aversive chemical stimuli, turns may be co-modulated with saccades, and this could in theory manifest in several different yet mutually non-exclusive ways. For example, as S-T events likely mediate turns, the proportion of saccade-coupled tail flips can be increased. In addition, kinematic coordination during S-T events can be enhanced to make more pronounced turns. On the other hand, turns and forward gliding can also be modulated independent of S-T coordination, by altering the overall tail flip asymmetry and undulation interval of tail flips. To test these possibilities, we used potent and ethologically representative appetitive or aversive chemical stimuli determined by the previous valence assays, including the death-associated diamines (Cad and Put) and the food-related amino acids (Val and Ala), each at a concentration of 1 mM (**Figure 1c**). Each of these chemicals and a blank control were precisely administered to larval zebrafish for a duration of 10 seconds in a pseudorandomized order with resting intervals during neural-behavioral imaging sessions (**Figure 4a,** see **Methods**).

We first examined the effects of chemical stimuli on saccade, putative turn and forward motion individually. Only the aversive chemicals led to a higher saccade frequency and a lower tail flip frequency during their presentation (**Figures 4b–d**), both of which returned to baseline levels shortly after the cessation of stimulation (**Figures 4c, d**). Consistently, pre-tail flip intervals were the longest during aversive stimuli, and shortest in the presence of appetitive chemicals (**Figure 4e**). During aversive stimuli, the proportion of saccade-coupled tail flips increased (**Figure 4f**), along with an increase in tail flip asymmetry (**Figure 4g**). In contrast, appetitive stimuli did not lead to any discernible change in tail flip asymmetry (**Figure 4g**). To examine whether larvae may intend to perform more forward swims in response to any chemical stimulus, we analyzed tail flips with ≥ 4 undulation cycles. We observed that only appetitive stimuli significantly increased the average undulation of these tail flips (**Figure 4h**), presumably leading to more sustained forward gliding movements [55]. Overall, although the

individual effects on saccades, tail flips, and stimulus trials appeared modest (**Figures 4b–h**), the cumulative impact of these discrete motor actions could effectively achieve the overarching behavioral goals of pursuit or avoidance.

In the presence of chemical stimuli, the saccades and tail flips during S-T events followed the same temporal and directional alignments (**Supplementary Figure 4**). Tail flips of S-T events during chemical stimuli also exhibited kinematic characteristics distinct from the flanking independent counterparts (**Supplementary Figures 5a–c**). These substantiate a conserved relationship between saccade and body turn. Notably, during aversive chemical-associated S-T events, we observed strong correlations between the magnitude of tail flip asymmetry and various temporal coupling parameters. Specifically, larger tail flip asymmetries were associated with shorter latencies between saccade and tail flip onsets and offsets (**Figures 4i, j**), longer durations of overlap between saccades and tail flips (**Figure 4k**), and longer durations of both individual saccades and tail flips (**Figures 4l, m**). Such correlations were absent among S-T events that occurred during blank control or appetitive chemicals (**Figures 4i–m**). These were also not observed when correlating average undulations with the temporal parameters for either appetitive or aversive chemical-associated S-T events (**Supplementary Figures 5d–h**). Furthermore, tail flip asymmetry, but not average undulation, was larger when an aversive chemical-associated S-T event occurred closer to the stimulus onset (**Supplementary Figures 5i, j**). These indicate a heightened coordination between saccades and tail flips specifically in response to aversive stimuli, where tightly synchronized saccade-tail flip events facilitate more intense turning actions.

Taken together, the two opposite chemical valences elicit distinct coordinated behavioral responses in larval zebrafish. Aversive chemicals lead to an increase in saccades and a higher proportion of enhanced, temporally coordinated saccade-coupled tail flips (**Figure 4n**), whereas appetitive chemicals result in more effective forward gliding movements without changes in saccade patterns or tail flip coupling (**Figure 4o**). These highlight the flexibility of the eye-body coordination system in zebrafish larvae, adapting to different chemical cues.

Pallial neuronal subsets are highly co-tuned to S-T events and chemical aversiveness

By analyzing the concurrently recorded brain-wide neuronal activities (**Figures 5a, b**), we aimed to identify neuronal ensembles involved in the control of coupled saccade-tail flips. To this end, we first designed motor regressors for each larva (see **Methods**). By calculating the mutual information (M.I.) between neuronal activity and these regressors, we identified neurons encoding spontaneous tail flips, and determined their preferential involvement in independent vs. saccade-coupled tail flips (see **Methods** for definition of motor preference). This analysis revealed that motor neurons across the brain generally exhibited a preference for independent tail flips, with a notable concentration in key motor command centers, specifically the brainstem mesencephalon and rhombencephalon [56,57] (**Figures 5c, d**). Interestingly, neurons in the telencephalic pallium, a homolog of the cortex in more complex vertebrates [58], displayed the weakest preference for independent tail flips and the strongest preference for S-T events, compared to other brain regions (**Figures 5c, d**).

We then examined the spatial distributions of chemical valence-encoding neurons (**Supplementary Figure 6**) (see **Methods** for definition of valence preference). Among the

primary projection target regions of the olfactory bulbs in the telencephalon [59,60], we observed distinct activation patterns in response to aversive and appetitive chemicals (**Figures 5e, f, Supplementary Figures 6**). Aversive chemical-elicited activities are channeled through both the pallium and subpallium, whereas appetitive chemicals are well-represented in the subpallium (**Supplementary Figures 6a–d**). This subpallial appetitive preference mirrors the reported stronger response to mating water compared with skin extract in the juvenile zebrafish subpallium [30]. In most downstream regions, positive valence was represented by larger numbers of neurons (**Figures 5e, f, Supplementary Figures 6a–d**). In parallel to its preference for spontaneous S-T events in motor control, the pallium also exhibited a more pronounced representation of negative valence compared with other brain regions (**Figures 5e, f**). Of note, although neurons involved in spontaneous S-T event and negative valence representation were outnumbered, they exhibited significantly higher activation levels compared with the counterparts encoding independent tail flips and positive valence, respectively (**Supplementary Figures 7a, b**).

Next, we analyzed the neuronal sensorimotor preferences to understand how individual neurons encode both motor actions and chemical valence (**Figures 5g–k**). For each neuron, we calculated a joint preference measure as the L^2 norm of a two-dimensional vector consisting of the two preference measures (i.e., [motor preference, valence preference], used in **Figures 5c, e**) (see **Methods** for details). We used the measure to quantify a neuron's preferential responsiveness to either S-T events combined with aversive stimuli, or independent tail flips combined with appetitive stimuli. This analysis further illustrated that the pallium exhibited the strongest overall preferential co-encoding of spontaneous S-T events and negative valence (**Figures 5h, i, Supplementary Figures 7c, d**). In contrast, more caudal brain regions better co-represent spontaneous independent tail flips and positive valence (**Figures 5j, k**).

Putative pallial involvement in amplifying coordinated eye-body turns

We further examined the temporal dynamics of pallial activity in relation to chemical cue-associated S-T events. Specifically during aversive cues, pallial motor-encoding neurons exhibited early activation preceding tail flip onset in S-T events, but not during appetitive chemicals presentation (**Figure 6a, *upper*, Supplementary Figure 8**). This was also noted in rhombomeres 4 and 6 (**Supplementary Figure 8**), but not in the other brain regions (**Figure 6a, *upper*, Supplementary Figure 8**).

In the telencephalon, pallial motor activations were more prominent for aversive chemical-associated S-T events with a higher temporal proximity of saccade and tail flip onsets (**Figure 6a, *lower*, Supplementary Figure 9a**), or aversive chemical stimulus and tail flip onsets (**Supplementary Figure 9b**). This neural activity pattern aligns with the behavioral observations that tail flip asymmetry inversely correlated with saccade-tail flip onset delay (**Figure 4i**), as well as aversive chemical-associated S-T event onset delay from stimulus onset (**Supplementary Figure 5i**). Interestingly, these were not observed for rhombomeres 4 or 6, where the early motor activations appeared independent of these event proximities (**Supplementary Figures 9a, b**). These observations indicate a sensorimotor role for pallial motor-encoding neurons, potentially mediating the increase in tail flip asymmetry and strengthening of saccade-tail flip coupling by aversive cues. In contrast, the activation patterns

in rhombomeres 4 and 6 suggest a premotor role for subsets of neurons in these hindbrain regions, possibly driving S-T events independently of their temporal proximity to the initiation of aversive chemical stimulus.

In contrast to S-T events, independent tail flips exhibited distinct associated neuronal activity patterns. These were characterized by a lack of early pallial activation relative to tail flip onset during aversive cues presentation (**Figure 6b, Supplementary Figure 10**). Instead, independent tail flips were associated with early neuronal activations in the preoptic area, pretectum, tectum, rhombomere 7, and caudal hindbrain, particularly during appetitive stimuli (**Supplementary Figure 10**). This differential activation pattern further underscores the unique role of pallium in coordinating S-T events, especially in response to aversive stimuli.

Collectively, these findings align with and provide a neural basis for the aversive chemical-specific enhancement of saccade-tail flip coordination observed behaviorally (**Figures 4i–m, Supplementary Figure 5i**). They also highlight the larval zebrafish pallium as a key sensorimotor hub in integrating sensory information and motor outputs (**Figure 6c**).

Discussion

Chemosensation is one of the most ancient and conserved sensory mechanisms, playing a critical role in guiding locomotion and body orientation across the animal kingdom [26]. While its influence on body movements is well-documented, our study provides the first direct evidence that chemosensory inputs modulate eye-body coordination, a dynamic interplay previously thought to rely primarily on visual and mechanosensory cues. Using larval zebrafish as a model system, we uncovered a sensory-motor integration mechanism wherein chemosensory valence shapes not only locomotor behaviors but also the temporal and directional coupling of saccades and body turns. These findings reveal a previously unknown synergy between oculomotor and chemosensory systems, expanding our understanding of how multisensory integration drives adaptive motor control.

Larval zebrafish swim and make body turns in discrete bouts, a behavior that reflects a foundational motor pattern common in many animal species during development [61]. We show that saccades and tail flips are tightly coupled in a more complicated manner than previously known, with saccade direction aligning with peak body turn magnitude. This temporal and directional coordination likely optimizes visuomotor behaviors such as tracking and orienting, which are essential for survival. Chemosensory valence further modulates this coordination: aversive cues enhance saccade-tail coupling, driving sharper turns and more frequent saccade-coupled movements, while appetitive cues promote forward gliding with minimal impact on saccade-tail coupling. These distinct motor programs may facilitate context-specific responses, such as more efficient predator evasion, or foraging in favorable environments. This modulation of visuomotor coordination by chemosensory input aligns with conserved principles of motor control described in other vertebrates, such as in *Xenopus laevis*, where eye and body movements are synchronized via feedforward efferent copies of spinal central pattern generator activity. In general, such multi-modal information integration should help to ensure gaze stability and locomotor efficiency. However, a limitation on the interpretation of our findings, is that the observed increase in saccade-tail coupling during aversive stimulation may arise indirectly from increased saccade frequency rather than a direct modulation of coupling

by aversive cues. Further investigation, disentangling the contributions of saccades and tail flips, would clarify the mechanism underlying this increased coordination.

At the neuronal circuit level, we identified the telencephalic pallium as a key region integrating chemosensory valence with motor program execution. Negative chemical valence was strongly represented in olfactory circuits and downstream relay regions, suggesting that aversive cues engage specific sensorimotor pathways to enhance saccade-coupled turns. The pallium, a homolog of the mammalian cortex [58], likely plays a central role in gating chemosensory-driven motor responses. Recent studies have highlighted the pallium's multifaceted functions, including sleep regulation [62], place encoding [63] and spatial representations [64]. Our findings add to this body of work by demonstrating its role in integrating sensory valence with motor output, even at an early developmental stage. This underscores the pallium's importance as a hub for adaptive motor control in vertebrates.

The evolutionary implications of these findings are significant, indicating that the ability to integrate chemosensory input with motor programs likely emerged over 450 million years ago [65]. By revealing how chemosensory valence modulates eye-body coordination, our study sheds light on the conserved nature of sensory-motor integration. This mechanism may be present across other vertebrates, though species-specific adaptations—such as the absence of necks in teleost fish [42,43]—likely shape and determine species-specific patterns of coordination. In mammals or birds, for instance, head and neck movements may play a more prominent role in sensorimotor integration.

This work opens avenues for further studies on sensory input-mediated eye-body control. First, the neuronal circuits underlying chemosensory modulation of eye-body coordination should be explored in greater detail. High-resolution imaging of specific brain regions, such as the pallial and subpallial structures, could reveal how chemosensory valence is encoded and transformed into motor commands. Second, extending these studies to other species, including vertebrates with flexible necks, could provide insights into how evolutionary pressures have shaped sensorimotor integration. Third, investigating additional sensory modalities (e.g., auditory [66]) and their interactions with chemosensation may uncover more general principles of multisensory integrations.

In conclusion, our findings reveal a new mechanism by which chemosensory cues modulate eye-body coordination, providing insights into the neural basis of adaptive locomotion. By integrating behavioral and neuronal findings within an evolutionary framework, this work advances our understanding of sensory-motor integration and lays the foundation for future studies on multisensory control of motor behaviors.

Key resources table

REAGENT or RESOURCE	SOURCE	IDENTIFIER
Chemicals		
Valine	Sigma, USA	94619
Alanine	Sigma, USA	05129
Prostaglandin F2α	Cayman, USA	CAY16010
Cadaverine	Sigma, USA	D22606
Putrescine	Sigma, USA	51799
Chenodeoxycholic acid	Sigma, USA	C9377
Glycodeoxycholic acid	Sigma, USA	06863
Adenosine	Sigma, USA	A9251
Sodium Chloride	Sigma, USA	59888
SU-8 2150 Photoresist	Microchem, USA	N/A
Sylgard™ 184 Silicone Elastomer Kit	Dow Corning, USA	N/A
IR dye	Sigma, USA	543349
Deposited data		
Code	This paper	https://github.com/khsamuelsy/ChemoEyeTailMvmnts/
Data	This paper	Will be made available upon acceptance of the manuscript
Freely moving arena data	Sy et al. [27]	https://doi.org/10.5281/zenodo.7306139
Experimental models: Organisms/strains		
Tg(elavl3:GCaMP6f)	Engert Lab	N/A
Tg(elavl3:H2B-GCaMP7f)	Randlett Lab	N/A
Software and algorithms		
Streampix 7	www.norpix.com	RRID:SCR_015773
AutoCAD 2020	www.autodesk.com	RRID:SCR_021072
MATLAB R2018b	www.mathworks.com	RRID:SCR_001622
Custom zebrafish tracking	Sy et al. [27]	https://github.com/khsamuelsy/FishChip
Variational Stationary Noise Remover (VSNR)	Fehrenbach et al. [67]	https://www.math.univ-toulouse.fr/~weiss/Codes/VSNR/VSNR.zip)
NoRMCorrE	Pnevmatikakis et al. [68]	https://github.com/flatironinstitute/NoRMCorre
CaImAn	Giovannucci et al. [69]	https://github.com/flatironinstitute/CaImAn-MATLAB

Other		
Syringe pump	Longerpump, Beijing	LSP02-2A
Transfer tubing	Cole-Parmer, USA	6417-21; 6417-41
IR illumination	TMS, Malaysia	ANGX-1000-CH1-24V
CCD camera	Allied Vision, Germany	Mako G-040B PoE
Silicon wafer	Semiconductor Wafer, Taiwan	N/A
Solenoid valve	Lee Company, USA	LHDA0533115H
Laser	Crystalaser, USA	DL-488-050-0
Cylindrical lens	Thorlabs, USA	LJ1695RM-A
Galvanometric mirror	Thorlabs, USA	GVS211/M
F-theta lens	Sill Optics, Germany	S4LFT0061/065
Tube lens	Thorlabs, USA	TTL200-A; TTL200-B
Excitation objective	Nikon, Japan	N10X-PF
Detection objective	Thorlabs, USA	TL10X-2P
Electrically tunable lens	Optotune, Switzerland	EL-16-40-TC-VIS-20D-1-C
Lens controller	Gardasoft, UK	TR-CL-180
sCMOS camera	PCO, Germany	Panda 4.2
Multifunctional I/O device	National Instruments, USA	PCIe-6323

Methods details

Animals

All experimental procedures received prior approval from the Animal Research Ethical Committee of the Chinese University of Hong Kong (CUHK) and complied with the Guide for the Care and Use of Laboratory Animals. For this study, *nacre*-mutant larvae, aged 5–8 days post-fertilization (d.p.f.), were raised and maintained under a 14-hour light/10-hour dark cycle at a constant temperature of 28°C. Larvae used for experiments were not fed, as per common practice and this does not compromise their health at this developmental stage [70]. The larvae used in the valence determination assay (n = 313) were bred from adult zebrafish pairs with at least one heterozygous Tg(elavl3:GCaMP6f) parent and were not screened for GCaMP6f expression. The larvae used in the behavioral and neuronal imaging assays (n = 5) were bred from Tg(elavl3:H2B-GCaMP7f) adults and were screened for the presence of GCaMP7f expression. The sex of larvae was not determined at this stage of development.

Fluidics-based swimming arena for chemical valence determination

The device was designed using AutoCAD 2020 (Autodesk, USA) and comprised five 1.5 mm-thick layers of laser-engraved poly(methyl methacrylate) (PMMA). The layers were meticulously aligned vertically and fused by applying a chloroform solution along the contact edges, which yielded a durable, sealed structure. This process formed a closed square arena with dimensions of 40 mm in length and 1.5 mm in height (**Figure 1a**). An additional inlet was used for loading larvae and sealed prior to assays. The inlets and outlets are 200 µm wide, prohibiting larvae from exiting the arena through these channels. Fluidic connections were established by securing syringe needles (Terumo, USA) to the topmost PMMA layer with an epoxy adhesive paste (Devcon, USA). These needles were linked to the inlet and outlet channels, which in turn connected to syringes containing the fluid stimuli and to a waste collection bottle, respectively. The connections were facilitated using poly(tetrafluoroethylene) (PTFE) tubing (Cole-Parmer, USA). After construction, the device was left to air-dry for 24 hours, allowing for the complete evaporation of residual chloroform and epoxy adhesive paste. To ensure the device was contaminant-free, it was washed thoroughly with water twice, thus removing any potential contaminants prior to its use in behavioral assays.

Defined chemical zones within the arena were created using four fluid streams, each channeled through inlet channels located at the corners of the arena and propelled at a constant flow rate of 100 µL/min by syringe pumps (LSP02-2A, Longerpump, Beijing). The background solvent of these fluid streams was either water or a 0.5% DMSO solution, depending on the tested chemical species. In total, 9 chemicals were tested, including valine (Val; Sigma, USA), alanine (Ala; Sigma, USA), prostaglandin F2α (PGF2α; Cayman, USA), cadaverine (Cad; Sigma, USA), putrescine (Put; Sigma, USA), chenodeoxycholic acid (CDCA; Sigma, USA), glycodeoxycholic acid (GDCA; Sigma, USA), adenosine (Ade; Sigma, USA), and sodium chloride (NaCl; Sigma, USA). Chemicals with limited water solubility, including PGF2α, CDCA, and GDCA, were dissolved in 0.5% DMSO solution to ensure complete dissolution. This concentration of DMSO has been determined to be safe for the larvae and does not affect their baseline behaviors [71]. Other chemicals were dissolved in water.

The top right control quadrant (quadrant I) contains no chemicals, while the remaining quadrants contain chemical species at varied concentrations (**Figures 1a, b**). For the three chemical species with limited solubility, both water and 0.5% DMSO were used as controls in separate assays (**Supplementary Figures 1b, c**). The outlet of the arena was connected to an open waste collection bottle to allow for the efficient disposal of the outflow fluids.

The Reynolds number (*Re*) of fluid flow in the arena is given by $Re = \rho v D_H/\mu$, where ρ is the fluid density, v is the fluid flow velocity, D_H is the hydraulic diameter of the device, and μ is the fluid dynamic viscosity. Given the average cross-sectional dimensions at each quadrant of the arena (i.e., 1.5 mm × $10\sqrt{2}$ mm), the corresponding average flow rate was 100 μL min^{-1} or 1.67 mm^3 s^{-1}. Hence the average flow velocity = 1.67 mm^3 s^{-1}/(1.5 mm × $10\sqrt{2}$ mm) = 7.86×10^{-5} m s^{-1}. D_H for the rectangular channel is given by $2ab/(a+b) = 2.71 \times 10^{-3}$ m, where a and b are the average dimensions of the rectangular cross-sections (i.e., 1.5 mm and $10\sqrt{2}$ mm). Substituting the D_H found, and the density (996 kg m^{-3}) and the dynamic viscosity (8.32×10^{-4} Pa.s) of water at 28 °C, the Reynolds number was found to be $Re = 0.255 << 2000$. As $Re << 2000$, the streams were laminar with negligible mixing [72] and static fluid zone borders were formed. The Péclet number (*Pe*) of fluid flow in the arena is given by $Pe = vD_H/D$, where D is the diffusion coefficient of the molecule. Since all the investigated small molecules have diffusion coefficients of the 10^{-9} m^2s^{-1} range order, $Pe \approx 2.13 \times 10^2 >> 1$, the molecules thus have minimal diffusivity across the streams. The *Re* and *Pe* values suggest that the chemicals delivered using the system would be minimally crossing via advection and diffusion, respectively, and therefore stay highly localized within individual fluid streams. As the geometry and flow profile of the four quadrants are identical, four identical static chemical zones are established. The chemical zones were visualized by infusing an IR dye (IR 806, Sigma, USA) into the quadrant II and IV of the device (**Figure 1a, *lower***).

Chemical valence determination assay

During a chemosensory valence determination assay, three to six zebrafish larvae aged 5–8 days post fertilization (d.p.f.) were placed in a swimming arena and allowed to acclimate for 15 minutes before the introduction of chemical stimuli. To minimize potential visual cues across different assays, the arena was horizontally rotated to a single angle of 0°, 90°, 180°, or 270° in a pseudo-randomized manner for each assay. To further reduce these cues, the recording was conducted under 850-nm IR illumination (ANGX-1000-CH1-24V, TMS, Malaysia) in the absence of visible light. Time-lapse video was recorded by a CCD camera (Mako G-040B PoE, Allied Vision, Germany) at 20 frames per second, with image acquisition managed by Streampix 7 (Norpix, Canada). The recording lasted for 30 minutes, with four fluid streams flowing at the same speed. The fluid temperature was maintained at ~28°C throughout the assay. This assay enables precise behavioral monitoring of the larvae, ensuring that the specific chemical exposure was exactly known, thereby minimizing potential biases in hedonic measurements.

Microfluidic device for multichannel precise chemical simulation, saccade, tail flip and brain-wide cellular-resolution imaging

Capturing the behaviors and neural activity elicited by chemosensory cues presents a significant challenge in the field. In our previous development of Fish-On-Chips [27], we enhanced the precision of a single chemical cue delivery to larval zebrafish, enabling stable recordings of neuronal responses to chemosensory inputs. In this work, we further developed the platform with the objective of systematically exploring the impact of multiple ecologically pertinent, valence-inducing chemicals on the natural behaviors of larval zebrafish and uncovering the associated neural circuitry.

Compared with our previous device, we further optimized the channel design in order to achieve multiple chemical delivery, compatibility with dual-scanning light sheet imaging and maximize the behavioral readout to include both saccade and tail flip. The PDMS-based microfluidic device was designed in AutoCAD 2020 (Autodesk, USA). It was then fabricated by customized photolithography techniques like the previous ones to incorporate flat transparent sidewalls at the front and the right side with respect to the head chamber to accommodate for the entry of two scanning excitation light sheets, and a thin glass ceiling for the emitted fluorescence detection path. Briefly, a 2D design was printed on a soda lime mask (Supermask, Shenzhen). Negative photoresist SU-8 2150 (Microchem, USA) was spin-coated on a 4-inch silicon wafer (Semiconductor Wafer, Taiwan) to 500-μm thick. The device pattern was then transferred to the photoresist with UV exposure (OAI, USA), followed by post-exposure bake and etching to produce a master mold. Mixed PDMS (Dow Corning, USA) and curing agent (at 10:1 w/w) were poured into the salinized mold to a thickness of 5 mm, with perpendicular glass slides held upright on the mold to produce the front and the right side flat vertical surfaces upon curing. After solidification at either 65°C for 240 minutes or 100 °C for 60 minutes, it was detached from the mold, bonded and sealed onto a microscopic cover slide (as thin glass ceiling) by plasma treatment. All devices were rinsed with water twice before use in experiments.

The fluidic stream control solution was similar to our previous design. In brief, bilateral three-layered, sandwiched fluid streams are directed to the larval zebrafish from the sides and converge at the middle, and then leave the device. The middle stream was switched to different solutions to allow selections of chemicals in different trials. Each fluid stream was carried by PTFE tubes, controlled by a solenoid valve (LHDA 0533115H, Lee Company, USA), and driven by a syringe pump. A side channel connecting the chemical delivery microchannels and the tail chamber was incorporated to buffer pressure changes in the fluidic environment, and minimize mechanical disturbances to the larval subject. The flow rate was uniformly adjusted at 80 μL/min, which yields the same order magnitude of *Re* and *Pe* numbers, and thus allows for highly controlled fluid delivery. The details of the valve control and chemical delivery are described in the following sections.

Through iterative experimentation, we determined the necessity for bilaterally independent channels to achieve symmetrical stimulus rise and fall times. One challenge we noted was the natural formation of micro-sized air bubbles during fluid coalescence, which can interfere with the accuracy of fluid delivery. The likelihood of bubble formation scales with the number of fluid inlets. We optimized the design to include a total of 7 channels on each

side, using the first and last channels for water streams (sandwiching the chemical streams), and 5 channels dedicated to different chemical streams (**Figure 1d**).

These significant enhancements, together with other minor ones, enabled us to systematically deliver 4 different water-soluble chemicals plus 1 blank water control for 4–6 repeated trials each. We ensured a 10-second exposure duration for each stimulus trial to allow sufficient time for the larval subjects to exhibit saccadic and tail flipping responses, which differed greatly in event frequency. Additionally, we also ensured a 10-second imaging time after each stimulus was removed. This setup was optimal for multi-trial simultaneous behavioral-neuroimaging experiments, allowing for approximately one hour total assay time per larval subject. We anticipate incorporating additional channels and an even more streamlined experiment paradigm with further developments.

Dual-scanning light sheet fluorescence microscope for whole-brain calcium imaging

We custom-built a light sheet fluorescence microscope with two light sheet excitation paths from the front and right side of the larval subject for optimized cellular-resolution whole-brain imaging. For each of the excitation paths**,** a 486 nm-centered blue gaussian laser (DL-488-050-0, Crystalaser, USA) was used as the excitation light source. The laser beam was resized to 0.6 mm in diameter ($1/e^2$) by a pair of telescopic lenses (LB1757-A, LB1596-A, Thorlabs, USA), which then passed through a scanning system, followed by a cylindrical lens (LJ1695RM-A, Thorlabs, USA) that focused the horizontal dimension of the parallel beam onto the back focal plane of an air excitation objective (Nikon Plan Fluorite, ×10, N.A. 0.3, 16 mm WD). This expanded the laser horizontally to form a light sheet. The scanning system consisting of a galvanometric mirror (GVS211/M, Thorlabs, USA), a F-theta lens (S4LFT0061/065, Sill Optics, Germany) and a tube lens (TTL200-A and TTL200-B, Thorlabs, USA) was used to scan the light sheet vertically and linearly over a range of 276 µm. The F-theta and tube lenses also expanded the beam 3.31 times, resulting in a beam diameter of 2 mm ($1/9^{th}$ of the objective back aperture) and effective excitation N.A. of 0.0332. A photomask with a 250 µm aperture and a photomask with an open-ended aperture (**Supplementary Figure 2d**) were placed and aligned at the front and at the right side of the device respectively to avoid directly shining the eyes of the larval subject with either light sheet at either side.

Along the detection path, a bandpass green filter (525 ± 25 nm) was placed after an air detection objective (TL10X-2P, Thorlabs, USA; ×10, N.A. 0.5, 7.77 mm WD) to block the blue excitation light. An electrically tunable lens (EL-16-40-TC-VIS-20D-1-C, Optotune, Switzerland) was linearly driven by a lens controller (TR-CL-180, Gardasoft, UK) and synchronized with the light sheet scanner to achieve rapid focusing of different image planes onto the sensor of a sCMOS camera (Panda 4.2, PCO, Germany). During an experiment, to correct for axial drift, a reference plane was calibrated with respect to the initial measurement at the beginning of each trial. All control units were synchronized using a multifunctional I/O device (PCIe-6323, National Instruments, USA) and custom-written codes in MATLAB (R2018b, MathWorks, USA).

Simultaneous whole-brain calcium imaging and behavioral recording

To obtain the most naturalistic data, we only included larvae that were nearly perfectly leveled in the device (evidenced by the two eyes at the same level) for further experimentation and analysis. A total of five larvae aged 5–6 days post fertilization (d.p.f.) from three batches of breedings were included. Each of the five robustly behaving zebrafish larvae underwent simultaneous behavioral and whole-brain neuronal calcium imaging experiments in an upright orientation as permitted by the improved imaging set-up.

In an imaging experiment, a larva was loaded (via the larva inlet) and fitted into the trapping chamber of the PDMS-based microfluidic device using a syringe pump and monitored under a surgical microscope. Then, the larva was allowed to acclimate for 15 minutes. Introduction of bubbles to the microfluidic system was carefully minimized during system setup to avoid unwanted fluid flow pattern changes or mechanical instability of the larval subject. Prior to functional imaging, a detailed anatomical stack of the larval zebrafish brain spanning 138 imaging planes at 2-μm intervals was taken. In this intact upright imaging configuration, the majority of the brain except the topmost (e.g., habenula) and bottommost regions (e.g., caudal hypothalamus) which are directly under the cover glass slide and furthest from the detection objective lens, was consistently imaged across larvae.

During functional imaging, whole-body saccadic and tail flipping behaviors (single-plane, at 200 Hz) and volumetric whole-brain calcium fluorescence signals (28 planes with 7-μm intervals, at 2 Hz) were simultaneously imaged under chemosensory cue (or blank control) delivery. Behavioral images were acquired under IR illumination by a CCD camera (Mako G-040B PoE, Pike, Germany) and the Streampix 7 (Norpix, Canada) image acquisition software, while calcium images were acquired with the abovementioned custom dual-light sheet scanning microscope. Each larva underwent 23–30 experimental trials with a total of five types of stimuli. These stimuli include amino acids (valine and alanine), diamines (cadaverine and putrescine), all at one millimolar concentration, and a blank control. Each stimulus was delivered bilaterally to both nostrils for 4–6 repetitions. Each trial lasted for 50 seconds with 30-second baseline, 10-second stimulus presentation, and 10-second post-stimulus recording periods, followed by ~90-second inter-trial resting intervals. Axial drift corrections were then performed in between trials.

During each 30-second baseline recording period, in the three-layer sandwiched fluid streams, the middle stimulus stream carried a chemical cue (or water for blank control trials). The first (water) and the second (stimulus) stream in front of the nostrils were then switched off sequentially by the respective controlling valves at the two sides, with 10-second gap to allow the second (stimulus) and the third stream (water) to contact the nostrils. This resulted in the initiation and termination of chemical stimulation. Recording continued for 10 seconds after stimulus cessation.

Valence determination analysis (swimming arena)

Individual frames of the navigation behavioral tracking videos were first registered for translation, background-subtracted, and contrast-adjusted. The *xy*-coordinates of the heads of larvae in each frame were extracted using our previously established semi-automated template matching-based tracking program [27] custom-written in MATLAB (R2018b, MathWorks, US). All tracking results were manually verified on a frame-by-frame basis and corrected when

necessary. The coordinates were then used to calculate the proportions of time spent in each of the same-area quadrants over the 30-minute recording time. Additionally, since there is minimal mixing across streams under laminar flows, interactions between quadrants containing the same chemical at different concentrations were negligible. The population standard deviation of the time spent difference in chemical quadrants (compared with the control quadrant) of the setup was estimated from the sample standard deviation of the time spent difference in the control group with Bessel's correction.

Behavioral image processing and analysis (microfluidic device)

Eye and tail movements were extracted from behavioral images by a custom MATLAB program (R2018b, MathWorks). The first ten seconds of the behavioral recordings of each trial were excluded from analysis to avoid confounding behaviors evoked by the onset of light sheet illumination. In addition, a total of six trials, three trials each from two subjects, were found to have bubbles present, which disrupted the laminar flows necessary for precise chemical delivery. These trials were also discarded. For eye movements, the video was down-sampled by a factor of 25 times (resultant frame rate: 8 fps) to achieve a higher signal-to-noise ratio. The turn direction and duration of the saccades were manually identified using rotational visual flows in each region-of-interest of the two eyes. Only two events (out of 595 events recorded from 5 larvae) of bilateral eye movements from one larva were recorded with incoherent eye movement directions, and these were excluded from analysis. Pre-saccade interval was defined as the time between the onset of a saccade and that of its preceding one, if both were recorded.

For tail movements, episodes of tail flips were identified based on changes in tail tip-waist angle using several criteria. An episode was isolated when tip-waist angle changes occurred in at least two consecutive frames (frame rate: 200 fps), and were temporally situated before and after at least three frames of stationary angle changes. The start and end frames were determined as the last frame of the last idle period and the first frame of the next idle period, respectively. Positive and negative peaks in the undulating cycles of angle changes were identified using the built-in *findpeaks* function in MATLAB (R2018b, MathWorks, USA). The undulation cycle was determined by averaging the number of positive and negative peaks.

Pre-tail flip interval was defined as the time between the onset of a tail flip and that of its preceding one, if both were recorded. Tail flip duration was calculated as the time difference between the end and start frame of an episode. The average undulation was calculated by dividing the duration by the undulation cycle. Magnitude and tail flip asymmetry were calculated using the sum and difference of the average net positive and average net negative peaks, respectively, with the zero reference being the average of the start and end angles (**Supplementary Figure 3f**). A small non-zero average tail flip asymmetry to the right side was consistently observed in the spontaneous tail flips of the five subjects (2.6° ± 1.2° (mean ± S.D.)), which was due to the asymmetrical illumination from the right side. Tail flip asymmetry calculation was adjusted by subtracting each subject's average tail flip asymmetry.

Tail flips were classified based on tail flip asymmetry. A tail flip with an asymmetry of ≥ 1.5° (one-half of the median asymmetry of all spontaneous tail flips) was considered a turn event. If the asymmetry was < 1.5°, it was classified as a non-turn event. In the laterality analysis of tail flips (**Figures 2f, h, Supplementary Figures 3e, 4e, g, l, n, s, u**), only turn

events were included for comparisons. Non-turn events, indicating forward movement, were excluded from this analysis.

A tail flip was defined as saccade-coupled (S-T events) if the onset occurred within 0.5 seconds of a saccade's onset (i.e., |T-ON - S-ON| ≤ 0.5 seconds). For each saccade, only the tail flip with the closest onset was considered saccade-coupled. S-T events with saccade onset certainly later than the tail flip onset, defined as those with T-ON - S-ON < -0.0625 seconds with the temporal error of saccade time determination considered, represented a small subset (11 out of 172) of all spontaneous S-T events (**Figure 2b**). This pattern was largely conserved for chemical-associated S-T events (appetitive: 4 out of 33, aversive: 3 out of 32, **Supplementary Figures 4h, o).** These were not included for the regression analysis of S-T coordination (**Figures 4i–m, Supplementary Figures 5d–j**).

Events recorded during blank trials were classified as spontaneous. During chemical stimulation trials, events were considered spontaneous if the onset was recorded before the stimulus onset, and the offset was recorded before or coincided with the stimulus onset. Events were considered to be stimulus-evoked if the onset occurred later than stimulus onset, and the offset occurred before or coincided with the stimulus offset. Onset and offset of S-T events were defined as that of the saccade. Events during the resting intervals between trials were not recorded or analyzed.

Pre-event interval was defined as the time difference between the onset of a saccade, a tail flip, or a bout and that of the respective preceding one (**Figures 1e, 2d, e, 3a, 4e, Supplementary Figures 2b, 3g, i, j, 5c**). For comparison with flanking events (**Figures 2d, e, g–j, Supplementary Figures 3k, l**), saccades and tail flips were first categorized into either S-T or independent groups and set as the 0th next event. For each 0th next event, the sequence and quantity of other events (n^{th} next event) were shown. An event could be the 1st next event for one sequence and the 2nd next event for another, causing overlaps.

Comparative analysis based on previously acquired data of freely swimming larvae

A dataset from our previous study was used [27]. In that study, 11 larvae in 3 assays were allowed to swim in the absence of visible light for 2 hours in a 2D rectangular arena (60 mm × 30 mm × 1.5 mm) completely filled with still water, and imaged under IR illumination. The heading orientation (10° resolution) of every larva in each frame was extracted using a semi-automated template matching-based tracking program custom-written in MATLAB (R2018b, MathWorks, US). All bouts subsequent to the first bout in the rightmost virtual chemical zone of the arena were extracted for analysis. Pre-bout interval was defined as the time difference between the onset of a swim bout and that of its preceding bout. Turn angle was defined as the orientation change in either direction. A swim bout was defined as a turn bout based on the turn angle being ≥ 70°, and non-turn bout otherwise. Only swim bouts with an orientation change were used to compare the proportion of consecutive ipsilateral turns (**Figures 3c, d**).

Calcium image processing and signal extraction

We adopted an analysis pipeline similar to our previous work [27]. Detailed larval zebrafish brain anatomical stacks were registered to the Z-Brain Atlas [73] using affine transformation followed by non-rigid image registration using custom scripts written in

MATLAB (R2018b, MathWorks, USA). Functional imaging planes were matched to the corresponding anatomical stack by maximization of pixel intensity cross-correlation and manually verified. Stripe artifacts in the anatomical stacks and functional imaging frames were removed using the Variational Stationary Noise Remover (VSNR) algorithm [67]. Functional imaging frames were motion-corrected using discrete Fourier transform and NoRMCorrE algorithms [68]. Trials with blurred frames due to in-frame drifts were discarded. Region of interest (ROIs) corresponding to individual neurons were then extracted using the CaImAn package [69]. Anatomical landmarks and the regional identity of each ROI were verified by manual inspection (by S.K.H.S.). Note that this only included neurons that had fired at least once during all imaging sessions and with a sufficiently high signal-to-noise ratio determined by the CaImAn-based analysis pipeline.

Trials with unsatisfactory image registration were excluded from further analysis. For one larva with more jitters in the functional images, the images stack were initially downsampled to 1 Hz by averaging every two consecutive frames. For trials with plane-specific jitters, a small proportion of frames with jitters were replaced with the immediate preceding frame (or the next frame if the preceding frame also had jitter) for the data from all larvae. Trials with more than two consecutive jittering frames were excluded from further analysis. In total, we retained whole-brain neuronal imaging data from 88 out of 139 trials from the five larvae that passed all quality control criteria.

Identification of motor- and sensory-coding neurons

The first 10.5 or 11 seconds (21 or 11 imaging frames) of the imaging data of each trial were excluded from analysis to avoid the inclusion of transient activity evoked by the onset of light sheet illumination. The minimum fluorescence intensity in the subsequent 4.5 or 4 seconds (9 or 4 imaging frames) of each ROI was used as the baseline fluorescence (F). The ΔF/F signals of the remaining imaging frames were calculated as the calcium response of each ROI.

Motor and sensory regressors were designed to identify motor- and sensory-encoding ROIs. Motor output was defined to be the proportion of frames with active tail flip in each 0.5-s or 1-s imaging time bin, and a motor output regressor was created to represent this (motor regressor 1). A second motor regressor for independent tail flips was created by excluding all tail flips of S-T events (motor regressor 2). A third regressor was designed by randomly removing tail flip events from motor regressor 1 at a probability that corresponded to each larva's S-T event proportion (motor regressor 3). Utilizing these three regressors allowed us to directly identify both the saccade-coupled and independent tail flip-encoding neurons but avoided saccade-encoding neurons [6,74]. Chemical stimulus regressors were created with a step function during the stimulus window of each chemical. All regressors are normalized to the [0, 1] range. We calculated the mutual information (I) between the calcium responses of each ROI and the regressors by a method based on kernel density estimation of the probability density functions of variables [75]. For motor mutual information, only all the imaging frames in the entire blank trials and before stimulus onsets in stimulus trials were used for calculation. For sensory mutual information , all imaging frames were used. With the three motor (**Table 1**) and five chemical stimulus regressors, each ROI had eight mutual information values, namely $I_{\text{tail_flip_all}}$ (based on motor regressor 1), $I_{\text{tail_flip_independent}}$ (based on motor regressor 2),

$I_{\text{tail_flip_randomRemove}}$ (based on motor regressor 3), as well as I_{valine}, I_{alanine}, $I_{\text{cadaverine}}$, $I_{\text{putrescine}}$, and I_{blank} (for which the suffix denotes the chemical or blank control). These values were used to determine significant motor and/or sensory information encoding, and calculate the motor and valence preferences (see the next sections).

Table 1. List of motor regressors and mutual information measures.

Regressor	Motor regressor 1, includes all tail flips	Motor regressor 2, excludes S-T events, i.e., all independent tail flips only	Motor regressor 3, excludes random tail flip events matching S-T proportion
Mutual information	$I_{\text{tail_flip_all}}$	$I_{\text{tail_flip_independent}}$	$I_{\text{tail_flip_randomRemove}}$

To estimate the distributions of the mutual information values expected under randomness, we shuffled the ΔF/F signals of each ROI (i.e., disrupting their temporal structures) and calculated another set of shuffled values. We defined the motor- and sensory-encoding neurons to be those that most significantly encode behavior variables or chemical stimuli. Motor-encoding neurons were defined as ROIs with either $I_{\text{tail_flip_all}}$ or $I_{\text{tail_flip_independent}}$ > 1.3 times 99th percentile of the shuffled $I_{\text{tail_flip_all}}$ or $I_{\text{tail_flip_independent}}$, respectively. Sensory-encoding neurons were defined as those with at least one I_{chemical} > 1.3 times the 99th percentile of the shuffled I_{chemical} (where the suffix refers to one of the four chemicals). ROIs with I_{blank} > 1.3 times the 99th percentile of the shuffled I_{blank}, representing neurons that putatively responded to valve and/or fluid velocity changes, were excluded. ROIs with both significant I_{valine} and I_{alanine} were defined as appetitive chemical-encoding neurons, and ROIs with both significant $I_{\text{cadaverine}}$ and $I_{\text{putrescine}}$ were defined as aversive chemical-encoding neurons. Valence-encoding neurons were defined as the union of appetitive and aversive chemical-encoding neurons.

Calculation of motor and valence preference for each neuron

Each of the mutual information values were normalized by dividing by the 99th percentile of the corresponding shuffled values (for simplicity of notation, hereafter referred to using the original symbols). Motor preference was defined for each motor-encoding neuron by the equation:

$$\text{Motor preference} = I_{\text{tail_flip_randomRemove}} - I_{\text{tail_flip_independent}}. \quad (1)$$

A higher value (> 0) of this quantity indicates stronger S-T event encoding, as mutual information kept after random tail flip removal (note the above-mentioned matching to S-T event proportion) is more than that with complete S-T removal. Conversely, a lower value (< 0) of such indicates stronger independent tail flip encoding, as more mutual information is kept with complete independent tail flip preservation than random removal that reduced independent tail flips while keeping some S-T events. Valence preference was defined for each sensory-encoding neuron by:

$$\begin{aligned}\text{Valence preference} &= \frac{I_{\text{cadaverine}} + I_{\text{putrescine}}}{2} - \frac{I_{\text{valine}} + I_{\text{alanine}}}{2} \\ &= I_{\text{aversive}} - I_{\text{appetitive}}.\end{aligned} \quad (2)$$

The norm of sensorimotor preferences was calculated for each unit of the union set of motor- and valence-encoding neurons that were S-T- and aversive valence-preferring (i.e., $I_{\text{tail_flip_randomRemove}} - I_{\text{tail_flip_independent}} > 0$ and $I_{\text{aversive}} - I_{\text{appetitive}} > 0$), or independent tail flip- and appetitive valance-preferring (i.e., $I_{\text{tail_flip_randomRemove}} - I_{\text{tail_flip_independent}} < 0$ and $I_{\text{aversive}} - I_{\text{appetitive}} < 0$) by the equation:

$$\text{Norm of sensorimotor preference} = \sqrt{\text{Motor preference}^2 + \text{Valence preference}^2}. \quad (3)$$

Data visualization

All smoothing was performed using the built-in *smooth* function in MATLAB (R2018b, MathWorks, USA), with span of moving average = 3 (**Figures 2e, h, i, j, 3b, d, e, and Supplementary Figures 3k, l**). In the time-series stimulus-evoked plots (**Figures 4c, d, f**), time bins were chosen as 5, 1.67, and 5 seconds, according to the event rates of saccade (**Figure 4c**), tail flip (**Figure 4d**) and S-T events (**Figure 4f**), respectively. Each bin includes the trailing but not the leading edge. Quantities were normalized by subtracting the average binned values in the 10-second pre-stimulus windows. Tail flip frequency was normalized to and expressed as the number of standard deviations of the binned pre-stimulus frequency (**Figure 4d**).

For the mean response of motor-encoding and valence-encoding ROI (**Supplementary Figures 7a, b**), each range includes the trailing but not the leading delimiter. For the motor response trace shown (**Figures 6a, b, Supplementary Figures 7a, 8–10**), the linear trend of ΔF/F before the tail flip event (t = -5s to -1s, 8 or 4 imaging frames) and the ΔF/F of the first time point (at t = -5s) were subtracted from all data points for the visualization of motor-triggered responses.

For brain regional average analysis, regions were included only if there were data from at least 3 larvae. As habenula and caudal hypothalamus were not consistently sampled (see above anatomical imaging section), these two regions were not included in any regional average plots (**Figures 5d, f, i, k, Supplementary Figures 6b, d, f, h, j, l, 8, 10**). Other regions without neurons from sufficient larvae that passed the sensory and/or motor function identification criteria (see above neuronal function identification sections) were also not included in some of these plots.

Statistics

In all plots, significance levels are set at $P < 0.05$. Significant P-values are shown in black font, while near-significant values are shown in gray font. In the imaging experiments, robust statistical power was achieved with data from 5 larvae. This was supported by the substantial number of events recorded, including 593 conjugate saccades and 1747 tail flips. Additionally, the total number of blank, appetitive and aversive trials used in statistical analyses were 28, 52 and 53 respectively.

For comparisons of time spent in the different quadrants in the valence determination assay (**Figure 1c**, **Supplementary Figures 1b, c**), two-sided Z-test with population standard deviation estimated from the sample standard deviation in the control group (i.e., water only in all quadrants) was used, followed by Benjamini-Hochberg procedure to control the false discovery rate across multiple comparisons. The comparisons were made across 7 cases,

including mean of individual, any 2, or all 3 chemical quadrants vs. mean of quadrant I. The most significant or near-significant *P*-values for each chemical are shown. In behavioral analysis, a two-sided Wilcoxon signed-rank test was used to assess whether the population median is zero (**Figures 2b, c and Supplementary Figures 3a, b, 4a–d, h–k, o–r**). Two-sided Wilcoxon rank-sum test was used to compare two sample sets (**Figure 1e, 2d, e, i, j, 3b, e and Supplementary Figures 3k, l**). For assessing expected proportions, two-sided binomial test was used (**Figures 2f, 3c, Supplementary Figures 3d, e, 4e–g, l–n, s–u**). One-sided Chi-squared test was used in comparing proportions between two groups (**Figures 2h, 3d**). For multiple group comparisons, Kruskal-Wallis test with Dunn-Sidak post hoc test was used (**Figures 4b–h**, **Supplementary Figures 5a–c**). Eta squared (η^2) is provided as a measure of effect size. For correlation analysis, either Spearman's rank correlation (**Supplementary Figures 3g–j**) or Pearson's correlation (**Figures 4i–m**, **Supplementary Figures 5d–j**) was used.

For comparisons in motor and valence preference, as well as the norm of motor and valence mutual information difference between the pallium and other brain regions, one-sided *t*-test was used (**Figures 5d, f, i, k**). Two-sided *t*-test was used to compare the mean positive valence mutual information between the pallium and the subpallium (**Supplementary Figure 6b**). To assess neuronal activation onset relative to motor event (**Figures 6a, b, Supplementary Figures 8–10**), right-sided *Z*-tests comparing pre-chemical cue-associated event neuronal activity at the two time points preceding the motor event to zero were performed. Significance was set at 2.5 standard deviations (S.D.), with S.D. estimated from spontaneous event baseline activity variability. Adjustment for multiple comparisons across time points and brain regions was made using the Benjamini-Hochberg procedure.

Data availability

Preprocessed data necessary to replicate these results will be made available upon publication of the manuscript.

Code availability

The custom code for data analysis is available on GitHub (https://github.com/khsamuelsy/ChemoEyeTailMvmnts/).

Acknowledgement

We thank Dorothy Ieong for zebrafish husbandry and technical support, and Anki Miu for administrative assistance for the project. We thank Owen Randlett for insightful discussions on the design of the project, and critical comments on the manuscript. Hui Zhao and Shen Gu for the provision of zebrafish larvae for equipment testing during initial protocol establishment. This work was supported by a Croucher Innovation Award (CIA20CU01) from the Croucher Foundation; the General Research Fund (14100122), the Collaborative Research Fund (C6027-19GF, C7074-21GF and C4062-22EF), and the Area of Excellence Scheme (AoE/M-604/16) of the RGC of UGC of Hong Kong; the Health@InnoHK program of the Innovation and Technology Commission of Hong Kong; the Excellent Young Scientists Fund (Hong Kong and Macau) (82122001) from the National Natural Science Foundation of China; the Asian Young Scientist Fellowship from the Future Science Awards Foundation; Margaret K. L. Cheung Research Centre for Management of Parkinsonism; the Lo's Family Charity Fund Limited; Gerald Choa Neuroscience Institute Research Program Fund.

Author contributions

Conceptualization: S.K.H.S., H.K.
Methodology: S.K.H.S., C.F., K.W., Y.M., Y.H., H.K.
Investigation: S.K.H.S., D.C.W.C., J.J.Z., J.L., C.F., Y.H., H.K.
Data Curation: S.K.H.S.
Formal Analysis: S.K.H.S.
Software: S.K.H.S., H.K.
Validation: S.K.H.S., H.K.
Visualization: S.K.H.S.
Supervision: H.K.
Project Administration: S.K.H.S., V.C.T.M., K.K.Y.W., H.K.
Funding Acquisition: V.C.T.M., K.K.Y.W., H.K.
Writing - Original Draft: S.K.H.S., D.C.W.C., H.K.
Writing - Review & Editing: All authors.

Competing interests

The authors declare no competing interests.

References

1. Dakin, R., Fellows, T. K. & Altshuler, D. L. Visual guidance of forward flight in hummingbirds reveals control based on image features instead of pattern velocity. *Proc Natl Acad Sci USA* 113, 8849–8854 (2016).
2. Byrne, R. A., Kuba, M. J., Meisel, D. V., Griebel, U. & Mather, J. A. Octopus arm choice is strongly influenced by eye use. *Behav. Brain Res.* 172, 195–201 (2006).
3. Bianco, I. H. & Engert, F. Visuomotor transformations underlying hunting behavior in zebrafish. *Curr. Biol.* 25, 831–846 (2015).
4. Land, M. F. Motion and vision: why animals move their eyes. *J. Comp. Physiol. A* 185, 341–352 (1999).
5. Srivastava, A., Ahmad, O. F., Pacia, C. P., Hallett, M. & Lungu, C. The Relationship between Saccades and Locomotion. *J. Mov. Disord.* 11, 93–106 (2018).
6. Wolf, S. *et al.* Sensorimotor computation underlying phototaxis in zebrafish. *Nat. Commun.* 8, 651 (2017).
7. Dowell, C. K., Lau, J. Y. N., Antinucci, P. & Bianco, I. H. Kinematically distinct saccades are used in a context-dependent manner by larval zebrafish. *Curr. Biol.* (2024) doi:10.1016/j.cub.2024.08.008.
8. Imai, T., Moore, S. T., Raphan, T. & Cohen, B. Interaction of the body, head, and eyes during walking and turning. *Exp. Brain Res.* 136, 1–18 (2001).
9. Lohnes, C. A. & Earhart, G. M. Saccadic eye movements are related to turning performance in Parkinson disease. *J Parkinsons Dis* 1, 109–118 (2011).
10. Lambert, F. M., Combes, D., Simmers, J. & Straka, H. Gaze stabilization by efference copy signaling without sensory feedback during vertebrate locomotion. *Curr. Biol.* 22, 1649–1658 (2012).
11. França de Barros, F. *et al.* Conservation of locomotion-induced oculomotor activity through evolution in mammals. *Curr. Biol.* 32, 453-461.e4 (2022).
12. Bacqué-Cazenave, J., Courtand, G., Beraneck, M., Lambert, F. M. & Combes, D. Temporal Relationship of Ocular and Tail Segmental Movements Underlying Locomotor-Induced Gaze Stabilization During Undulatory Swimming in Larval Xenopus. *Front. Neural Circuits* 12, 95 (2018).
13. Lavian, H., Prat, O., Petrucco, L., Štih, V. & Portugues, R. The representation of visual motion and landmark position aligns with heading direction in the zebrafish interpeduncular nucleus. *BioRxiv* (2024) doi:10.1101/2024.09.25.614953.
14. Sugioka, T., Tanimoto, M. & Higashijima, S.-I. Biomechanics and neural circuits for vestibular-induced fine postural control in larval zebrafish. *Nat. Commun.* 14, 1217 (2023).
15. Ehrlich, D. E. & Schoppik, D. A primal role for the vestibular sense in the development of coordinated locomotion. *eLife* 8, (2019).
16. Semmelhack, J. L. *et al.* A dedicated visual pathway for prey detection in larval zebrafish. *eLife* 3, (2014).
17. Mearns, D. S., Donovan, J. C., Fernandes, A. M., Semmelhack, J. L. & Baier, H. Deconstructing Hunting Behavior Reveals a Tightly Coupled Stimulus-Response Loop. *Curr. Biol.* 30, 54-69.e9 (2020).
18. Ahrens, M. B. *et al.* Brain-wide neuronal dynamics during motor adaptation in zebrafish. *Nature* 485, 471–477 (2012).
19. Naumann, E. A. *et al.* From Whole-Brain Data to Functional Circuit Models: The Zebrafish Optomotor Response. *Cell* 167, 947-960.e20 (2016).
20. Baden, T. Ancestral photoreceptor diversity as the basis of visual behaviour. *Nat. Ecol. Evol.* 8, 374–386 (2024).

21. Currier, T. A. & Nagel, K. I. Multisensory control of navigation in the fruit fly. *Curr. Opin. Neurobiol.* 64, 10–16 (2020).
22. Rössler, W. Multisensory navigation and neuronal plasticity in desert ants. *Trends Neurosci.* 46, 415–417 (2023).
23. Danilovich, S. & Yovel, Y. Integrating vision and echolocation for navigation and perception in bats. *Sci. Adv.* 5, eaaw6503 (2019).
24. Radvansky, B. A., Oh, J. Y., Climer, J. R. & Dombeck, D. A. Behavior determines the hippocampal spatial mapping of a multisensory environment. *Cell Rep.* 36, 109444 (2021).
25. Davis, S. N., Zhu, Y. & Schoppik, D. Larval zebrafish maintain elevation with multisensory control of posture and locomotion. *J. Exp. Biol.* (2025) doi:10.1242/jeb.250087.
26. Hoover, K. C. Smell with inspiration: the evolutionary significance of olfaction. *Am. J. Phys. Anthropol.* 143 Suppl 51, 63–74 (2010).
27. Sy, S. K. H. *et al.* An optofluidic platform for interrogating chemosensory behavior and brainwide neural representation in larval zebrafish. *Nat. Commun.* 14, 227 (2023).
28. Wakisaka, N. *et al.* An adenosine receptor for olfaction in fish. *Curr. Biol.* 27, 1437-1447.e4 (2017).
29. Hussain, A. *et al.* High-affinity olfactory receptor for the death-associated odor cadaverine. *Proc Natl Acad Sci USA* 110, 19579–19584 (2013).
30. Diaz-Verdugo, C., Sun, G. J., Fawcett, C. H., Zhu, P. & Fishman, M. C. Mating suppresses alarm response in zebrafish. *Curr. Biol.* 29, 2541-2546.e3 (2019).
31. Yabuki, Y. *et al.* Olfactory receptor for prostaglandin F2α mediates male fish courtship behavior. *Nat. Neurosci.* 19, 897–904 (2016).
32. Braubach, O. R., Wood, H.-D., Gadbois, S., Fine, A. & Croll, R. P. Olfactory conditioning in the zebrafish (Danio rerio). *Behav. Brain Res.* 198, 190–198 (2009).
33. Frank, T., Mönig, N. R., Satou, C., Higashijima, S.-I. & Friedrich, R. W. Associative conditioning remaps odor representations and modifies inhibition in a higher olfactory brain area. *Nat. Neurosci.* 22, 1844–1856 (2019).
34. Herrera, K. J., Panier, T., Guggiana-Nilo, D. & Engert, F. Larval zebrafish use olfactory detection of sodium and chloride to avoid salt water. *Curr. Biol.* 31, 782-793.e3 (2021).
35. Krishnan, S. *et al.* The right dorsal habenula limits attraction to an odor in zebrafish. *Curr. Biol.* 24, 1167–1175 (2014).
36. Doyle, W. I. & Meeks, J. P. Excreted steroids in vertebrate social communication. *J. Neurosci.* 38, 3377–3387 (2018).
37. Kadakia, N. *et al.* Odour motion sensing enhances navigation of complex plumes. *Nature* 611, 754–761 (2022).
38. Felsenberg, J., Barnstedt, O., Cognigni, P., Lin, S. & Waddell, S. Re-evaluation of learned information in Drosophila. *Nature* 544, 240–244 (2017).
39. Qiu, Q., Wu, Y., Ma, L. & Yu, C. R. Encoding innately recognized odors via a generalized population code. *Curr. Biol.* 31, 1813-1825.e4 (2021).
40. Iravani, B., Schaefer, M., Wilson, D. A., Arshamian, A. & Lundström, J. N. The human olfactory bulb processes odor valence representation and cues motor avoidance behavior. *Proc Natl Acad Sci USA* 118, (2021).
41. Yilmaz Balban, M. *et al.* Human responses to visually evoked threat. *Curr. Biol.* 31, 601-612.e3 (2021).
42. Kuroda, S., Lalonde, R. L., Mansour, T. A., Mosimann, C. & Nakamura, T. Multiple embryonic sources converge to form the pectoral girdle skeleton in zebrafish. *Nat. Commun.* 15, 6313 (2024).
43. Moyle, P. & Jr, J. C. *Fishes: An Introduction to Ichthyology*. 752 (Pearson, 2003).

44. Ahrens, M. B., Orger, M. B., Robson, D. N., Li, J. M. & Keller, P. J. Whole-brain functional imaging at cellular resolution using light-sheet microscopy. *Nat. Methods* 10, 413–420 (2013).
45. Nady, A., Peimani, A. R., Zoidl, G. & Rezai, P. A microfluidic device for partial immobilization, chemical exposure and behavioural screening of zebrafish larvae. *Lab Chip* 17, 4048–4058 (2017).
46. Mattern, K., von Trotha, J. W., Erfle, P., Köster, R. W. & Dietzel, A. NeuroExaminer: an all-glass microfluidic device for whole-brain in vivo imaging in zebrafish. *Commun. Biol.* 3, 311 (2020).
47. Candelier, R. *et al.* A microfluidic device to study neuronal and motor responses to acute chemical stimuli in zebrafish. *Sci. Rep.* 5, 12196 (2015).
48. van Giesen, L., Neagu-Maier, G. L., Kwon, J. Y. & Sprecher, S. G. A microfluidics-based method for measuring neuronal activity in Drosophila chemosensory neurons. *Nat. Protoc.* 11, 2389–2400 (2016).
49. Friedrich, R. W. & Korsching, S. I. Combinatorial and chemotopic odorant coding in the zebrafish olfactory bulb visualized by optical imaging. *Neuron* 18, 737–752 (1997).
50. Kim, D. H. *et al.* Pan-neuronal calcium imaging with cellular resolution in freely swimming zebrafish. *Nat. Methods* 14, 1107–1114 (2017).
51. Flash, T. & Hogan, N. The coordination of arm movements: an experimentally confirmed mathematical model. *J. Neurosci.* 5, 1688–1703 (1985).
52. Todorov, E. & Jordan, M. I. Smoothness maximization along a predefined path accurately predicts the speed profiles of complex arm movements. *J. Neurophysiol.* 80, 696–714 (1998).
53. *Anticipatory behavior in adaptive learning systems: foundations, theories, and systems*. vol. 2684 (Springer Berlin Heidelberg, 2003).
54. Dunn, T. W. *et al.* Brain-wide mapping of neural activity controlling zebrafish exploratory locomotion. *eLife* 5, e12741 (2016).
55. Gillis, G. B. Undulatory Locomotion in Elongate Aquatic Vertebrates: Anguilliform Swimming since Sir James Gray. *Am. Zool.* 36, 656–665 (1996).
56. Carbo-Tano, M. *et al.* The mesencephalic locomotor region recruits V2a reticulospinal neurons to drive forward locomotion in larval zebrafish. *Nat. Neurosci.* 26, 1775–1790 (2023).
57. Berg, E. M. *et al.* Brainstem circuits encoding start, speed, and duration of swimming in adult zebrafish. *Neuron* 111, 372-386.e4 (2023).
58. Mueller, T., Dong, Z., Berberoglu, M. A. & Guo, S. The dorsal pallium in zebrafish, Danio rerio (Cyprinidae, Teleostei). *Brain Res.* 1381, 95–105 (2011).
59. Kermen, F., Franco, L. M., Wyatt, C. & Yaksi, E. Neural circuits mediating olfactory-driven behavior in fish. *Front. Neural Circuits* 7, 62 (2013).
60. Korsching, S. I. Taste and smell in zebrafish. in *The senses: A comprehensive reference* 466–492 (Elsevier, 2020). doi:10.1016/B978-0-12-809324-5.24155-2.
61. Thelen, E. Rhythmical behavior in infancy: An ethological perspective. *Dev. Psychol.* 17, 237–257 (1981).
62. Leung, L. C. *et al.* Neural signatures of sleep in zebrafish. *Nature* 571, 198–204 (2019).
63. Yang, C. *et al.* A population code for spatial representation in the zebrafish telencephalon. *Nature* (2024) doi:10.1038/s41586-024-07867-2.
64. Fotowat, H., Lee, C., Jun, J. J. & Maler, L. Neural activity in a hippocampus-like region of the teleost pallium is associated with active sensing and navigation. *eLife* 8, (2019).
65. Brazeau, M. D. & Friedman, M. The origin and early phylogenetic history of jawed vertebrates. *Nature* 520, 490–497 (2015).
66. Veith, J. *et al.* The mechanism for directional hearing in fish. *Nature* 631, 118–124

(2024).
67. Fehrenbach, J., Weiss, P. & Lorenzo, C. Variational algorithms to remove stationary noise: applications to microscopy imaging. *IEEE Trans. Image Process.* 21, 4420–4430 (2012).
68. Pnevmatikakis, E. A. & Giovannucci, A. NoRMCorre: An online algorithm for piecewise rigid motion correction of calcium imaging data. *J. Neurosci. Methods* 291, 83–94 (2017).
69. Giovannucci, A. *et al.* CaImAn an open source tool for scalable calcium imaging data analysis. *eLife* 8, (2019).
70. Hernandez, R. E., Galitan, L., Cameron, J., Goodwin, N. & Ramakrishnan, L. Delay of initial feeding of zebrafish larvae until 8 days postfertilization has no impact on survival or growth through the juvenile stage. *Zebrafish* 15, 515–518 (2018).
71. Christou, M., Kavaliauskis, A., Ropstad, E. & Fraser, T. W. K. DMSO effects larval zebrafish (Danio rerio) behavior, with additive and interaction effects when combined with positive controls. *Sci. Total Environ.* 709, 134490 (2020).
72. Rhodes, M. *Introduction to Particle Technology*. 2nd edn. (1989).
73. Randlett, O. *et al.* Whole-brain activity mapping onto a zebrafish brain atlas. *Nat. Methods* 12, 1039–1046 (2015).
74. Ramirez, A. D. & Aksay, E. R. F. Ramp-to-threshold dynamics in a hindbrain population controls the timing of spontaneous saccades. *Nat. Commun.* 12, 4145 (2021).
75. Moon, Y. I., Rajagopalan, B. & Lall, U. Estimation of mutual information using kernel density estimators. *Phys. Rev. E Stat. Phys. Plasmas Fluids Relat. Interdiscip. Topics* 52, 2318–2321 (1995).

Figure 1

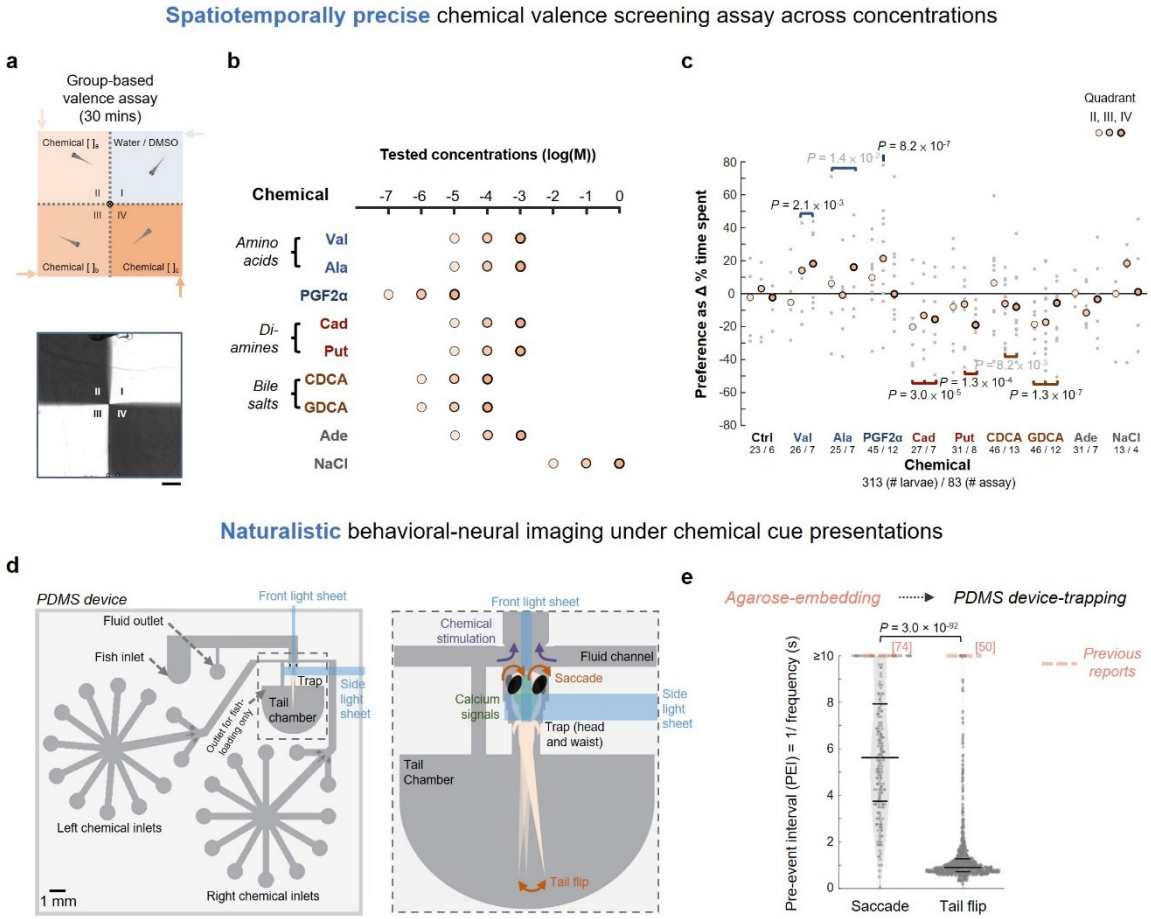
Spatiotemporally precise chemical valence screening assay across concentrations
a
Group-based valence assay (30 mins)
Chemical [ ]a
Water / DMSO
Chemical [ ]b
Chemical [ ]c
b
Tested concentrations (log(M))
Chemical
-7 -6 -5 -4 -3 -2 -1 0
Amino acids
Val
Ala
PGF2α
Di-amines
Cad
Put
Bile salts
CDCA
GDCA
Ade
NaCl
c
Quadrant
II, III, IV
Preference as Δ % time spent
P = 8.2 x 10-7
P = 1.4 x 10-3
P = 2.1 x 10-3
P = 8.2 x 10-3
P = 1.3 x 10-4
P = 3.0 x 10-5
P = 1.3 x 10-7
Ctrl 23 / 6
Val 26 / 7
Ala 25 / 7
PGF2α 45 / 12
Cad 27 / 7
Put 31 / 8
CDCA 46 / 13
GDCA 46 / 12
Ade 31 / 7
NaCl 13 / 4
Chemical
313 (# larvae) / 83 (# assay)
Naturalistic behavioral-neural imaging under chemical cue presentations
d
PDMS device
Front light sheet
Fluid outlet
Fish inlet
Trap
Tail chamber
Side light sheet
Outlet for fish-loading only
Left chemical inlets
Right chemical inlets
1 mm
Front light sheet
Chemical stimulation
Fluid channel
Saccade
Calcium signals
Side light sheet
Trap (head and waist)
Tail Chamber
Tail flip
e
Agarose-embedding
PDMS device-trapping
P = 3.0 x 10-92
[74]
[50]
Previous reports
Pre-event interval (PEI) = 1/ frequency (s)
Saccade
Tail flip

Figure 1. Fish-on-Chips 2.0 for studying chemosensation in larval zebrafish. (a) Upper panel: Schematic of the valence assay. Zebrafish larvae swimming in a two-dimensional arena (40 mm × 40 mm × 1.5 mm) are imaged at 20 fps under infrared (IR) illumination in the absence of visible light (see **Supplementary Figure 1a** for a more detailed schematic for the setup). Four quadrants with equal area are created and maintained by a constant, slow inflow of fluid at each corner (marked by arrows), with outflow occurring at a shared central outlet. The laminar flow maintains static borders between the zones. Lower panel: Visualization of the well-defined quadrants by infusing IR dyes into quadrant II and IV, and water into quadrant I and III. Scale bar: 5 mm. **(b)** Assayed chemicals and tested concentrations (varied across 3 consecutive orders of magnitude for each), including valine (Val), alanine (Ala), prostaglandin F2α (PGF2α), cadaverine (Cad), putrescine (Put), chenodeoxycholic acid (CDCA), glycodeoxycholic acid (GDCA), adenosine (Ade), and sodium chloride (NaCl). These were dissolved either in water or 0.5% DMSO and infused into quadrant II (lowest concentration) to IV (highest concentration). **(c)** Differences in % time spent in the chemical quadrants (i.e., II–IV, with different and increasing concentrations for each of the tested chemicals as indicated in **(b)** compared with the control quadrant (i.e., I), showing the values of individual assays (gray dots) and the medians (black-outlined dots). Below each chemical name, the first number indicates the total number of larvae assayed, and the second number specifies the total number of assays performed. *P*-values: Multiple *Z*-tests comparing different quadrant combinations' means to zero, with population standard deviation (S.D.) estimated from the sample S.D. of the control group (see **Methods**). Statistical significance after Benjamini-Hochberg adjustment: Black, significant; gray, near-significant. **(d)** Left panel: A drawing of the enhanced polydimethylsiloxane (PDMS)-based microfluidic device, featuring multiple chemical delivery channels on both sides of the larval head chamber. These channels are offset from the front to accommodate front excitation light sheet scanning, in addition to the right side light sheet. Right panel: A close-up illustration of the neural-behavioral imaging capabilities in a larval subject during precisely controlled chemical stimulus presentation. See **Supplementary Figure 2** for more details. **(e)** Pre-event intervals (PEIs) [1/ frequency] of spontaneous saccade and tail flip for all recorded events in the microfluidic device. Horizontal lines show the median, 25th and 75th percentiles for each group. $n = 5$ larvae with 216 spontaneous saccades and 1018 spontaneous tail flips, each with a recorded preceding reference event. Shaded areas scale according to the probability density function of values. *P*-value: Two-sided Wilcoxon rank-sum test. Dotted rose lines indicate the respective reduced frequencies in typical studies utilizing agarose-based embedding, both being < 0.1 Hz (see refs [50,74]).

Figure 2

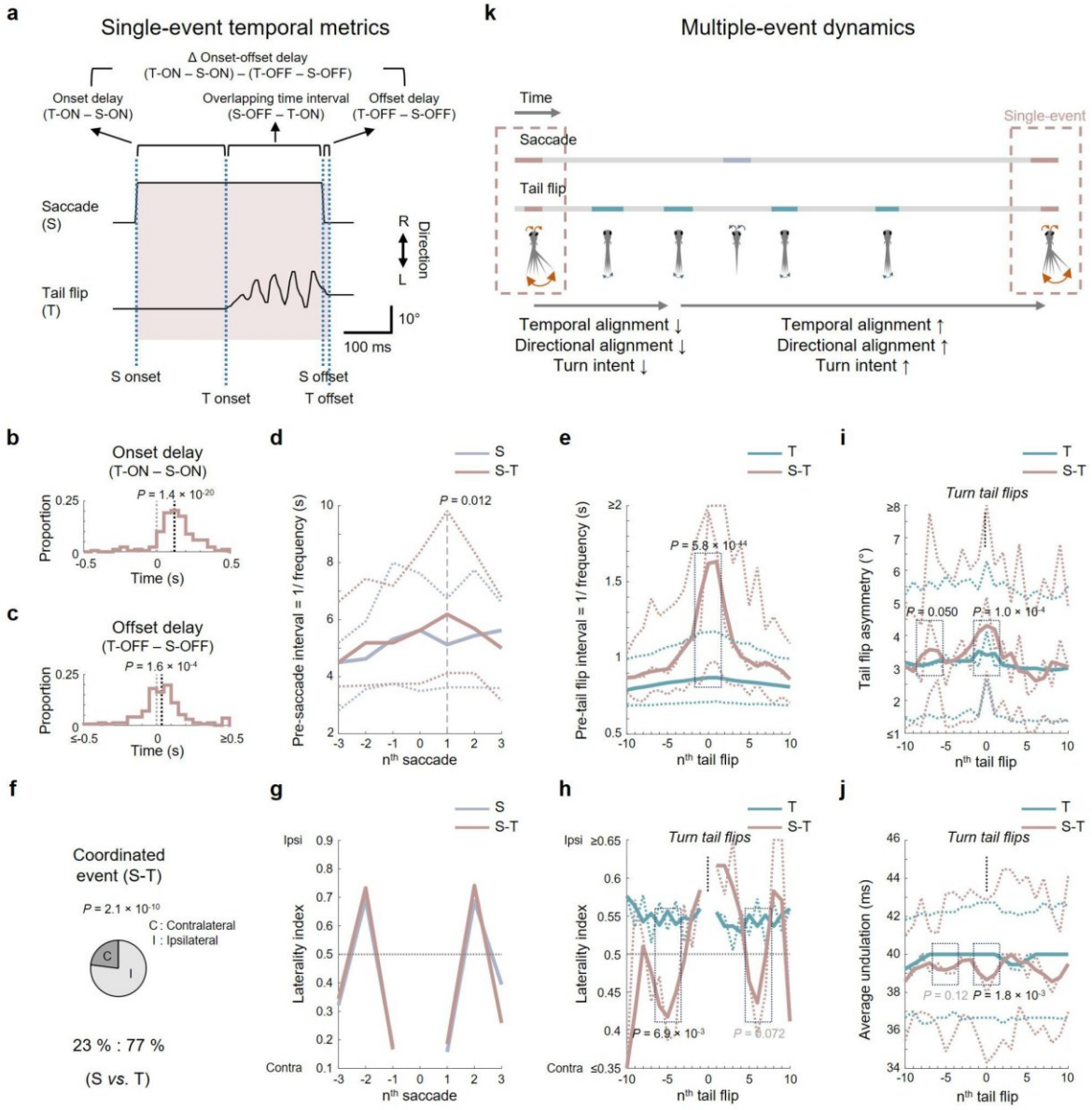
a
Single-event temporal metrics
Δ Onset-offset delay
(T-ON – S-ON) – (T-OFF – S-OFF)
Onset delay
(T-ON – S-ON)
Overlapping time interval
(S-OFF – T-ON)
Offset delay
(T-OFF – S-OFF)
Saccade
(S)
Tail flip
(T)
R
L
Direction
10°
100 ms
S onset
T onset
S offset
T offset
k
Multiple-event dynamics
Time
Saccade
Tail flip
Single-event
Temporal alignment ↓
Directional alignment ↓
Turn intent ↓
Temporal alignment ↑
Directional alignment ↑
Turn intent ↑
b
Onset delay
(T-ON – S-ON)
P = 1.4 × 10-20
Proportion
Time (s)
c
Offset delay
(T-OFF – S-OFF)
P = 1.6 × 10-4
d
S
S-T
P = 0.012
Pre-saccade interval = 1/ frequency (s)
nth saccade
e
T
S-T
P = 5.8 × 10-44
Pre-tail flip interval = 1/ frequency (s)
nth tail flip
i
Turn tail flips
P = 0.050
P = 1.0 × 10-4
Tail flip asymmetry (°)
f
Coordinated
event (S-T)
P = 2.1 × 10-10
C : Contralateral
I : Ipsilateral
23 % : 77 %
(S vs. T)
g
Ipsi
Contra
Laterality index
h
P = 6.9 × 10-3
P = 0.072
j
P = 0.12
P = 1.8 × 10-3
Average undulation (ms)

Figure 2. Tail flip dynamically aligns with saccade in rate and direction for performing spontaneous body turns. (a) Schematic illustrating the various temporal parameters of an example of coupled saccade-tail flip (S-T) event. **(b)** & **(c)** Histograms showing **(b)** onset delay and **(c)** offset delay of coupled saccade-tail flip (S-T) events. Note that the precision of measurements for the onset and offset for saccade and tail flip were 0.0625s and 0.0025s due to the respective sampling rates. Black and gray dashed lines indicate median and zero respectively. *P*-values: Two-sided Wilcoxon signed-rank test. **(d)** & **(e)** Pre-event intervals [1/ frequency] of self and flanking **(d)** saccades and **(e)** tail flips with respect to independent (S, saccade; T, tail flip) or S-T events. **(f)** Pie chart showing the proportions of contra- and ipsilateral turns, comparing the directionality of saccades (S) and tail flips (T; only turns considered, see **Methods**) in S-T events. *P*-value: Two-sided binomial test. **(g)** & **(h)** Laterality indices (defined as proportions of ipsilateral turns) in flanking **(g)** saccades and **(h)** turn tail flips (tail flip asymmetry ≥ 1.5°) with respect to independent (S, T) or S-T events. In **(h)**, the raw proportions (thin lines) and corresponding moving-average curves (thick lines) are shown. *P*-value: One-sided Chi-squared test comparing peaks and ± 1 events. **(i)** Tail flip asymmetry of self and flanking tail flips for independent tail flips (T) or S-T events with tail flip asymmetry ≥ 1.5° (see **Supplementary Figure 3k** for all events). **(j)** Average undulation of self and flanking tail flips for independent tail flips (T) or S-T events with tail flip asymmetry ≥ 1.5° (see **Supplementary Figure 3l** for all events). **(k)** Illustration of the temporal, directional and kinematic coordination of spontaneous saccades and tail flips. The temporal and directional alignment of tail flips with saccades, as well as their turning intent gradually decreases following a single S-T event and gradually increases preceding a single S-T event. Abbreviations in **(b)–(c)**, ON, onset; OFF, offset. In **(d)**, **(e)**, **(i)** & **(j)**, the thin curves represent the medians, 75th and 25th percentiles of all events. The raw median values (thin lines) and corresponding moving-average curves (thick lines) are shown in all these plots except **(d)**. *P*-values: Two-sided Wilcoxon rank-sum test comparing peaks and ± 1 events. For all plots, data were collected from n = 5 larvae, with 330 spontaneous saccades and 1,116 spontaneous tail flips.

Figure 3

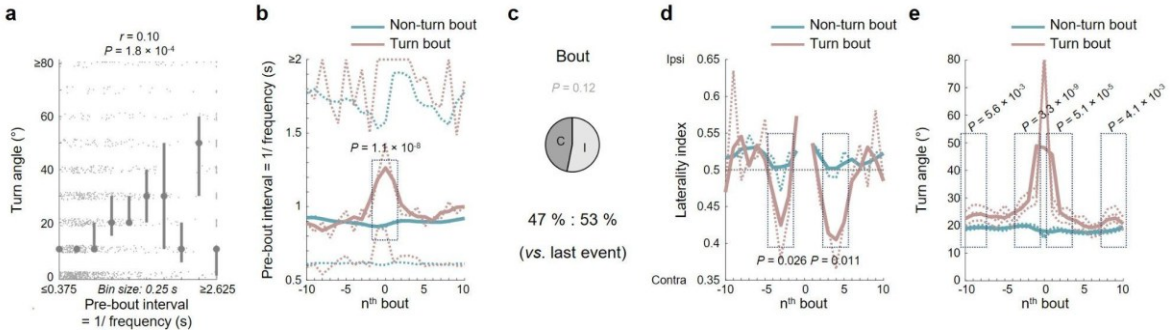

Figure 3. Freely moving zebrafish larvae dynamically align bouts in rate and direction for spontaneous body turns. (a) Medians and the 95% confidence intervals (based on bootstrapping with 1000 resamples) of the turn angle of all swim bouts vs. their pre-bout intervals (binned). Gray dots are individual data points. Turn angle values (sampled at an angular resolution of 10°) are slightly vertically dispersed for visualization. Spearman's rank correlation coefficients (*r*) and associated *P*-values are shown. **(b)** Pre-event interval [1/ frequency] of self and flanking swim bouts for non-turn (teal) or turn (coral) swim bouts (see **Methods**). Thin curves represent the raw median values, 75th and 25th percentiles. Thick curves are the moving-average of medians. **(c)** Pie chart showing the proportions of contra- and ipsilateral consecutive turns (i.e., comparing each swim bout to its preceding event). *P*-value: Two-sided binomial test. **(d)** Laterality index (defined as proportion of ipsilateral turn) in flanking swim bouts for non-turn (teal) or turn (coral) events. The raw median values (thin lines) and corresponding moving-average curves (thick lines) are shown. *P*-values: One-sided Chi-squared test comparing peaks and ± 1 events. **(e)** Turn angle of self and flanking tail flips for non-turn (teal) or turn (coral) swim bouts. The thin curves represent mean ± S.E.M. across time. The raw (thin lines) and corresponding moving-average curves (thick lines) for the mean are shown. In **(b)** & **(e)**, *P*-values: Two-sided Wilcoxon rank-sum test comparing peaks and ± 1 events. Note that however in **(e)**, the centered bout (i.e., 0th next bout) is by definition different and therefore only flanking bouts are compared. For all plots, data were collected from n = 11 larvae, with 1,529 spontaneous swim bouts.

Figure 4

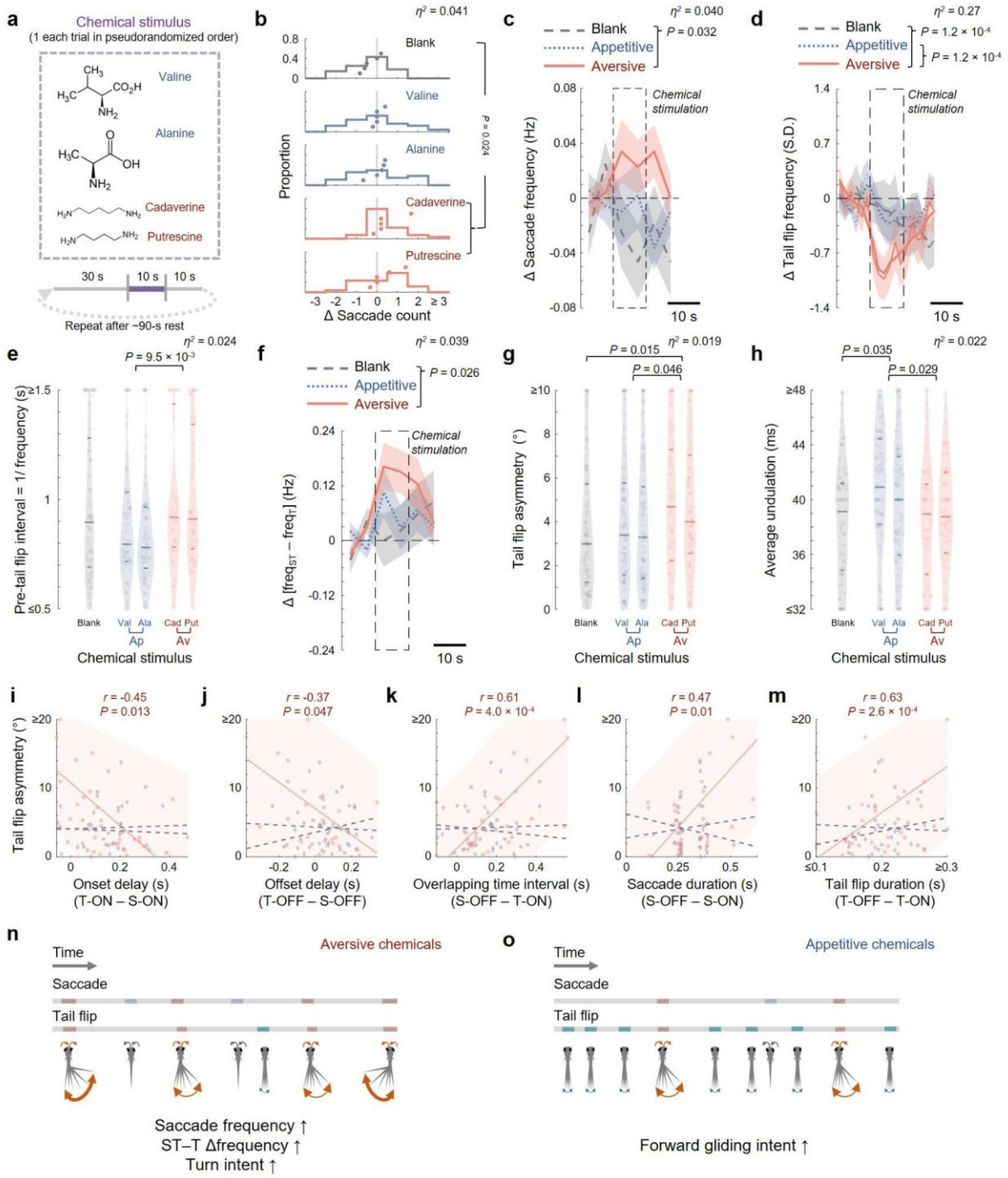
a
Chemical stimulus
(1 each trial in pseudorandomized order)
Valine
Alanine
Cadaverine
Putrescine
30 s
10 s
10 s
Repeat after ~90-s rest
b
η² = 0.041
Blank
Valine
Alanine
Cadaverine
Putrescine
P = 0.024
Proportion
Δ Saccade count
c
η² = 0.040
Blank
Appetitive
Aversive
P = 0.032
Chemical stimulation
Δ Saccade frequency (Hz)
10 s
d
η² = 0.27
P = 1.2 × 10⁻⁴
P = 1.2 × 10⁻⁴
Chemical stimulation
Δ Tail flip frequency (S.D.)
10 s
e
η² = 0.024
P = 9.5 × 10⁻³
Pre-tail flip interval = 1/ frequency (s)
Blank
Val Ala
Cad Put
Ap
Av
Chemical stimulus
f
η² = 0.039
Blank
Appetitive
Aversive
P = 0.026
Chemical stimulation
Δ [freq_ST − freq_T] (Hz)
10 s
g
P = 0.015
η² = 0.019
P = 0.046
Tail flip asymmetry (°)
Chemical stimulus
h
P = 0.035
η² = 0.022
P = 0.029
Average undulation (ms)
Chemical stimulus
i
r = -0.45
P = 0.013
Tail flip asymmetry (°)
Onset delay (s)
(T-ON – S-ON)
j
r = -0.37
P = 0.047
Offset delay (s)
(T-OFF – S-OFF)
k
r = 0.61
P = 4.0 × 10⁻⁴
Overlapping time interval (s)
(S-OFF – T-ON)
l
r = 0.47
P = 0.01
Saccade duration (s)
(S-OFF – S-ON)
m
r = 0.63
P = 2.6 × 10⁻⁴
Tail flip duration (s)
(T-OFF – T-ON)
n
Aversive chemicals
Time
Saccade
Tail flip
Saccade frequency ↑
ST–T Δfrequency ↑
Turn intent ↑
o
Appetitive chemicals
Time
Saccade
Tail flip
Forward gliding intent ↑

Figure 4. Aversive but not appetitive chemosensory cues amplify eye-body coordination via modulations of individual and joint movements of saccades and tail flips. (a) Illustration of chemical stimulation paradigm. During each trial, one appetitive or aversive chemical was administered to a tethered larval subject under neural-behavioral imaging. **(b)** Histograms showing the distributions of difference in saccade count between the 10-second stimulus window and the 10-second pre-stimulus period, across trials for each chemical and blank control. Each dot represents a trial-averaged saccade count change from a larva (dispersed vertically for visualization). **(c)** & **(d)** Stimulus-evoked changes in **(c)** saccade frequency and **(d)** normalized tail flip frequency (see **Methods**), compared with the pre-stimulus average. **(e)** Pre-tail flip interval [1/ frequency] of chemical stimuli-associated tail flips. **(f)** Stimulus-associated changes in the relative frequency of coupled saccade-tail flip (S-T) events vs. independent tail flips (i.e., Δ[S-T event frequency - independent tail flip frequency]) across time. **(g)** & **(h)** Kinematic parameters of chemical stimuli-associated tail flips including **(g)** tail flip asymmetry (all tail flips) and **(h)** average undulation (for tail flips with ≥ 4 undulation cycles). **(i)–(m)** Scatter plots of tail flip asymmetry vs. various temporal parameters for S-T events, including saccade-tail flip **(i)** onset delay, **(j)** offset delay, **(k)** overlapping time interval, **(l)** saccade duration, and **(m)** tail flip duration. Individual data points are shown in squares, diamonds and circles for the blank, appetitive and aversive groups respectively. **(n)** & **(o)** Illustrations of larval zebrafish behavioral changes upon **(n)** aversive and **(o)** appetitive chemicals presentations. In **(c)**, **(d)**, and **(f)**, quantities are binned and normalized to the average values in the 10-second pre-stimulus windows (see **Methods**). Lines and shadows show mean ± SEM (across trials). In **(d)**, the raw means (thin lines) and corresponding moving-average curves (thick lines) are shown. Dashed rectangles mark the stimulus window. In **(e)**, **(g)**, and **(h)**, horizontal lines indicate medians, 75th and 25th percentiles. Shadows of the violin plots scale according to the probability density function. In **(b)**–**(h)**, *P*-values: Kruskal–Wallis test with Dunn-Sidak post hoc test. Eta squared (η^2) is provided as a measure of effect size. In **(i)**–**(m)**, lines show best linear fits of each data group and shadows show 95% prediction confidence intervals of the aversive chemical data group (the only that exhibited significant associations). Pearson's correlation coefficients (r) and associated *P*-values are shown for the aversive chemical data points. Only data points with saccade onset certainly earlier than the tail flip onset were included in the regression analysis (see **Methods**). In **(l)**, saccade duration values (sampled at a temporal resolution of 0.125s) are slightly horizontally dispersed for visualization. Abbreviations: S, saccade; T, tail flip; ON, onset; OFF, offset; Ap, appetitive; Av, aversive. For all plots, data were collected from $n = 5$ larvae, and the total numbers of blank control, appetitive and aversive chemical trials used in statistical analyses are 28, 52 and 53, respectively. In **(d)**, the numbers of blank, appetitive and aversive trials with non-zero pre-stimulus tail flip frequency used in statistical analyses are 19, 34 and 27, respectively. In **(e)**, the total numbers of blank, appetitive and aversive events used in statistical analyses are 69, 130 and 89, respectively. In **(g)**, the total numbers of blank, appetitive and aversive events used in statistical analyses are 89, 167 and 124, respectively. In **(h)**, the total numbers of blank, appetitive and aversive events used in statistical analyses are 76, 156 and 111, respectively.

Figure 5

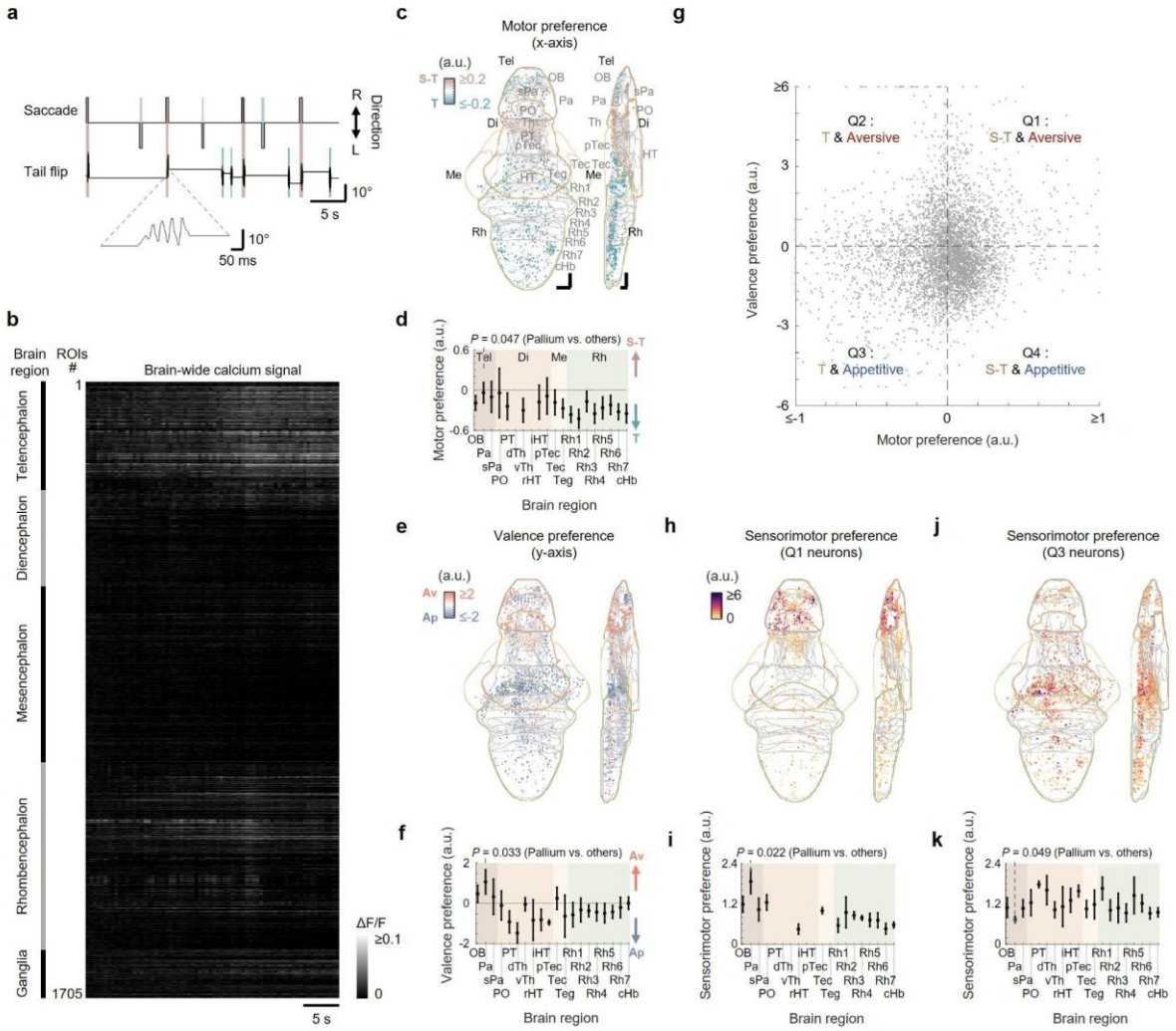
a
Saccade
Tail flip
R
L
Direction
10°
5 s
10°
50 ms
b
Brain region
ROIs #
Brain-wide calcium signal
Telencephalon
Diencephalon
Mesencephalon
Rhombencephalon
Ganglia
1
1705
5 s
ΔF/F
≥0.1
0
c
Motor preference (x-axis)
(a.u.)
S-T
≥0.2
T
≤-0.2
Tel
OB
sPa
Pa
PO
Di
Th
PT
pTec
HT
Me
Teg
Tec
Rh1
Rh2
Rh3
Rh4
Rh5
Rh6
Rh7
cHb
Rh
d
P = 0.047 (Pallium vs. others)
Motor preference (a.u.)
Brain region
e
Valence preference (y-axis)
(a.u.)
Av
≥2
Ap
≤-2
f
P = 0.033 (Pallium vs. others)
Valence preference (a.u.)
Brain region
g
Q2 : T & Aversive
Q1 : S-T & Aversive
Q3 : T & Appetitive
Q4 : S-T & Appetitive
Valence preference (a.u.)
Motor preference (a.u.)
h
Sensorimotor preference (Q1 neurons)
(a.u.)
≥6
0
i
P = 0.022 (Pallium vs. others)
Sensorimotor preference (a.u.)
Brain region
j
Sensorimotor preference (Q3 neurons)
k
P = 0.049 (Pallium vs. others)
Sensorimotor preference (a.u.)
Brain region

Figure 5. Pallial neuronal subsets are highly co-tuned to coupled saccade-tail flip (S-T) events and chemical aversiveness. (a) Heatmap of brain-wide spontaneous neuronal activities of a larval subject, acquired simultaneously with the motor outputs shown in **(b)**. **(b)** Spontaneous saccades and tail flips of the same larval subject in **(a)**, with a zoom-in example tail flip shown below. Temporally coupled saccade-tail flips (≤ 0.5s onset time difference) are indicated with coral blocks. Other saccades and tail flips are highlighted with blue and teal blocks, respectively. **(c)** Mean intensity projections (to transverse and sagittal planes) of motor preference of motor-encoding regions-of-interest (ROIs) (see **Methods**, x-axis in **(g)**). **(d)** Regional mean ± S.E.M. (across larvae) of motor preference. **(e)** Mean intensity projects (to transverse and sagittal planes) of valence preference for all valence-encoding ROIs (see **Methods,** y-axis in **(g)**). **(f)** Regional mean ± S.E.M. (across larvae) of valence preference. **(g)** Scatter plot of valence preference vs. motor preference of the union set of motor- and valence-encoding neurons. The four quadrants classify neurons into different sensorimotor tuning properties. **(h)** Mean intensity projections (to transverse and sagittal planes) of norm of sensorimotor preference (see **Methods**), for all ROIs preferring S-T event and aversive valence (i.e., quadrant I in **(g)**, also see **Supplementary Figure 7c** for zoom-in of the forebrain area). **(i)** Regional mean ± S.E.M. (across larvae) of norm of sensorimotor preference for all ROIs preferring S-T event and aversive valence. **(j)** Mean intensity projections (to transverse and sagittal planes) of norm of sensorimotor preference for all ROIs preferring independent tail flip and appetitive valence (quadrant III in **(g)**, also see **Supplementary Figure 7d** for zoom-in of the forebrain area). **(k)** Regional mean ± S.E.M. (across larvae) of norm of sensorimotor preference, for all ROIs preferring independent tail flip and appetitive valence. Scale bars in **(c)**: 50 μm in the Z-Brain Atlas space. In **(d)**, **(f)**, and **(i)**, *P*-values: Right-sided *t*-test comparing the pallium and non-pallial brain regions. In **(k)**, *P*-value: Left-sided *t*-test comparing the pallium and non-pallial brain regions. In **(c)**–**(f)** & **(h)**–**(k)**, the major brain regions (Tel: telencephalon, Di: diencephalon, Me: mesencephalon and Rh: rhombencephalon) are color-coded. Abbreviations of brain regions: OB olfactory bulb, Pa pallium, sPa subpallium, PO preoptic area, PT posterior tuberculum, dTh dorsal thalamus, vTh ventral thalamus, rHT rostral hypothalamus, iHT intermediate hypothalamus, pTec pretectum, Teg tegmentum, Rh1 rhombomere 1, Rh2 rhombomere 2, Rh3 rhombomere 3, Rh4 rhombomere 4, Rh5 rhombomere 5, Rh6 rhombomere 6, Rh7 rhombomere 7, cHb caudal hindbrain. Other abbreviations: S-T, coupled saccade-tail flip; T, independent tail flip; Ap, appetitive; Av, aversive. For all plots, the neural activity data correspond to the behavioral data reported in **Figures 2** & **4**, collected from $n = 5$ larvae.

Figure 6

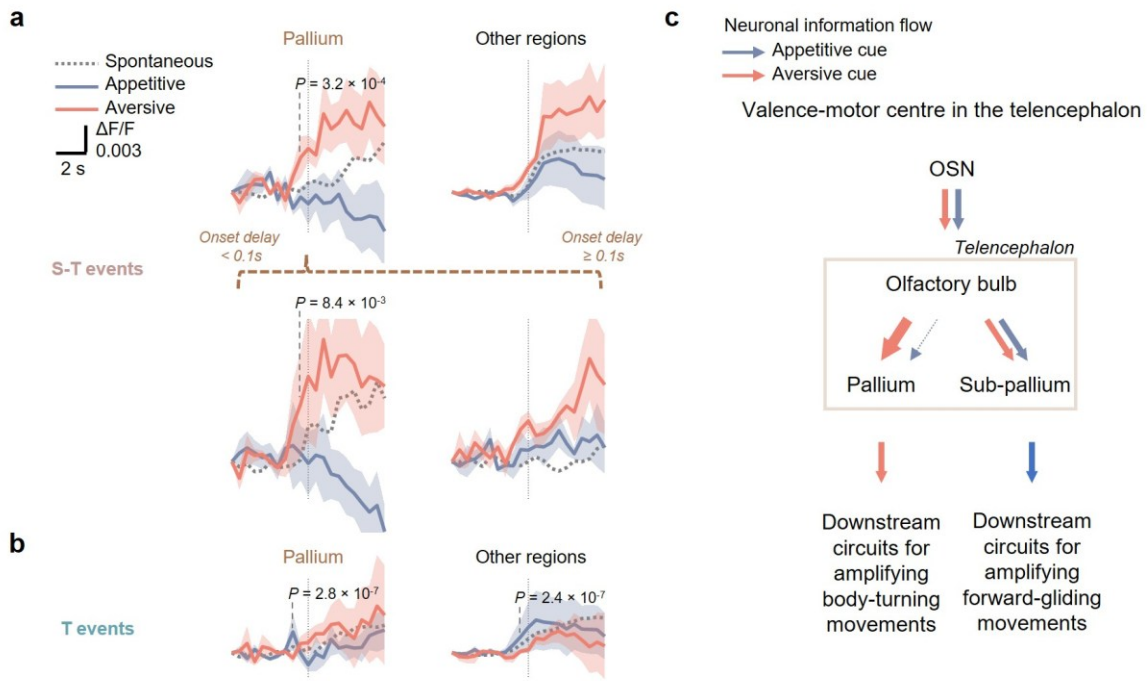

Figure 6. Pallial motor neuron activity onset precedes other brain regions during chemical cue-associated coupled saccade-tail flip (S-T) but not independent tail flip (T) events. (a) Upper panel: Mean ± S.E.M. (across larvae) responses of motor-encoding ROIs in the pallium (left) and non-pallial brain regions (right) to chemical cue-associated S-T events. Lower panel: Mean ± S.E.M. (across larvae) responses of motor-encoding ROIs in the pallium to chemosensory cue-associated S-T events with saccade-tail flip onset delay < 0.1 seconds (left) or ≥ 0.1 seconds (right). **(b)** Mean ± S.E.M. (across larvae) responses of motor-encoding ROIs in the pallium (left) and other brain regions (right) to chemical cue-associated independent tail flips. In **(a)** & **(b)**, dotted traces show the corresponding neuronal responses of spontaneous events. Dotted vertical lines indicate the time points of tail flip onsets (in a corresponding neuronal imaging frame). The neural activity data correspond to the behavioral data reported in **Figures 2** & **4**, collected from n = 5 larvae. P-values: Right-sided Z-tests comparing pre-chemical cue-associated event neuronal activity at each time point to zero. Significance was set at 2.5 standard deviations (S.D.), with S.D. estimated from spontaneous event baseline activity variability. Adjustment for multiple comparisons across time points and brain regions was made using the Benjamini-Hochberg procedure (see **Methods**). **(c)** Schematic illustrations showing the unique role of pallium in representing the transformation of negative chemical valence into initiation of amplified body-turning movements. Red and blue arrows represent the neuronal information flow for the processing of negative and positive chemical cue valence, respectively. Abbreviation: OSN, olfactory sensory neurons.

Supplementary Figure 1

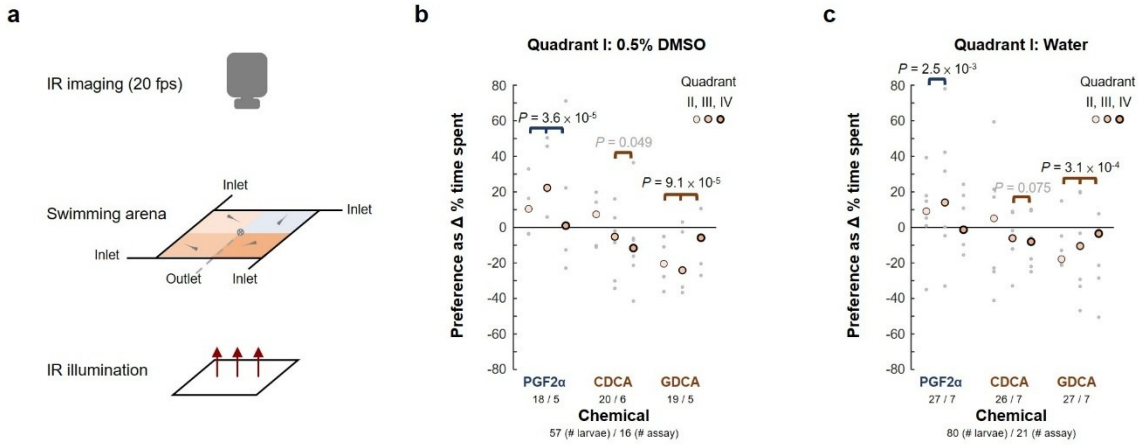

Supplementary Figure 1. Schematics and additional analysis of the valence determination assay. (a) Schematic of the valence determination assay. Zebrafish larvae swimming in a two-dimensional arena (40 mm × 40 mm × 1.5 mm) are imaged at 20 fps under infrared (IR) illumination in the absence of visible light. Four quadrants with equal area are created and maintained by a constant, slow inflow of fluid at each corner, with outflow at a shared central outlet. The laminar flow maintains static borders between the zones. **(b)** & **(c)** Differences in % time spent in the chemical quadrants (i.e., II–IV, with different and increasing concentrations for each of the tested chemicals as indicated in **Figure 1b**) compared with the water quadrant (i.e., I), showing the values of individual assays (gray dots) and the medians (black-outlined dots). The experiments were performed with either **(b)** 0.5% DMSO or **(c)** water in quadrant I. Below each chemical name, the first number indicates the total number of larvae assayed, and the second number specifies the total number of assays performed. *P*-values: multiple *Z*-tests across different quadrant combinations' means to zero, with population standard deviation (S.D.) estimated from the sample S.D. of the control group (see **Methods**). Statistical significance after Benjamini-Hochberg adjustment: Black, significant; gray, near-significant.

Supplementary Figure 2

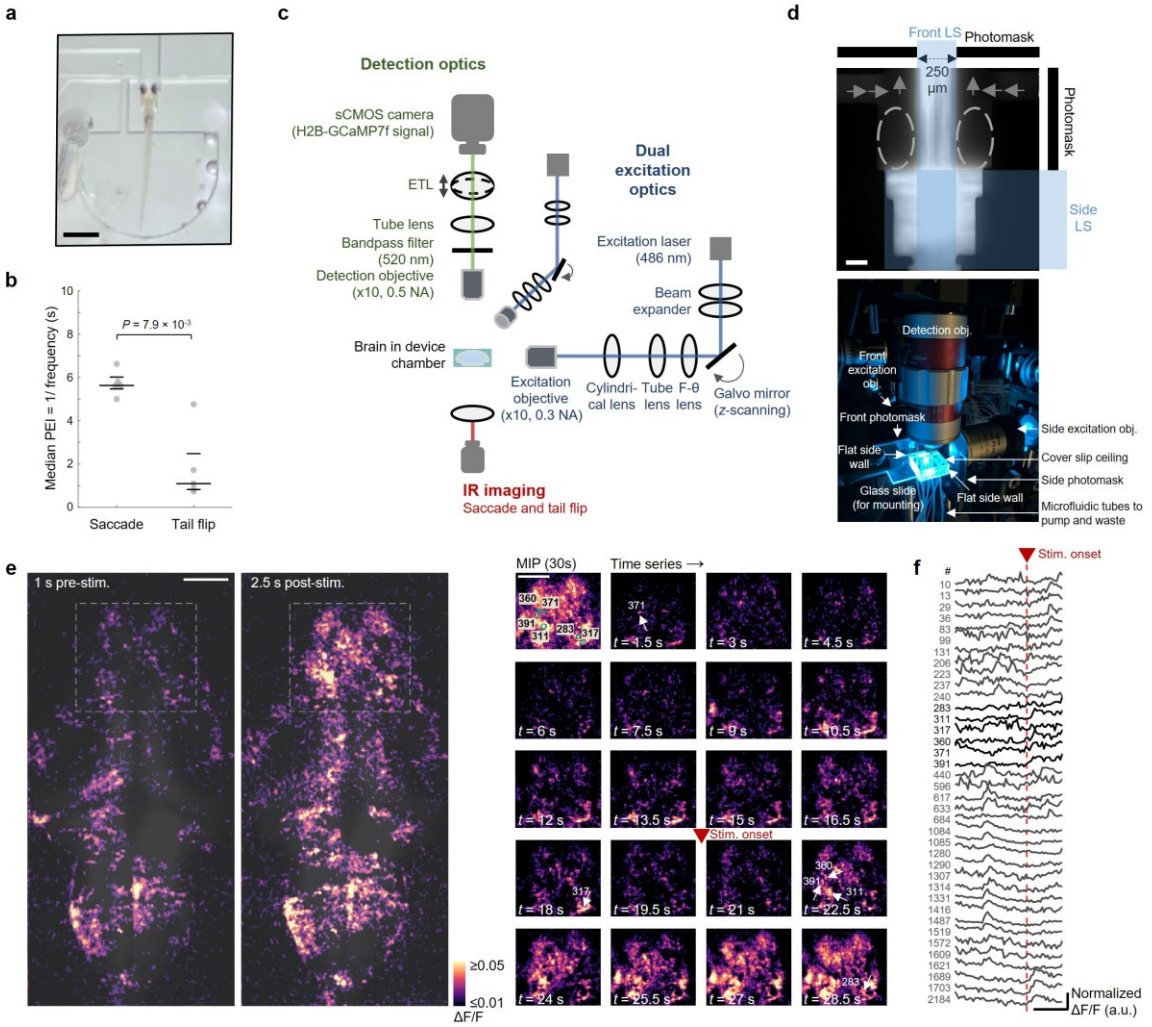

g

	Fish-on-Chip 1.0	Fish-on-Chip 2.0
Light sheet coverage	From the right only	From both the right and the front
Larval treatment/ orientation	Tilted or right-eye-ablated	Intact and upright
Recorded behavior	Tail movements only	Eye and tail movements
Tail flip frequency	Comparable to agarose-embedding	Comparable to freely moving

Supplementary Figure 2. More details on Fish-on-Chip 2.0: Enhanced platform for naturalistic behavioral-neural readouts in tethered larval zebrafish. (a) A photograph of a tethered larval zebrafish loaded into a PDMS-based microfluidic device (scale bar: 1 mm). Its eyes and tail are free to move while the head is fixed in place for fluorescence imaging. **(b)** Median pre-event intervals (PEIs) [1/ frequency] of spontaneous saccade and tail flip of each larva. Horizontal lines show the median, 25th and 75th percentiles for each group. $n = 5$ larvae with 216 spontaneous saccades and 1,018 spontaneous tail flips, each with a recorded preceding reference event. **(c)** Optical layout of the light sheet microscope, including two light sheet scanning modules which scan the larval brain from the side and the front respectively, a fluorescence detection module, and an IR imaging module for saccade and tail movements recording. **(d)** Upper panel: A fluorescence image showing sodium fluorescein in the microfluidic device excited by the front and side scanning light sheets (LS, illustrated by overlaid blue shadows), with photomasks placed to avoid the light sheets from directly reaching the larval eye positions (marked with white dashed ovals). A 250-µm window in the front photomask allows for the passage of the front excitation light to scan the brain regions between the eyes. Scale bar: 100 µm. Lower panel: A photograph showing the microfluidic device, objectives, and the associated tubings. **(e)** Left panel: An example functional image plane showing neural activation at two time points: before and after the presentation of 1 mM cadaverine. Anatomical reference images are overlaid. Right panel: A maximum intensity projection (MIP) and the time-series images of the first 30-second interval, focusing on a zoomed-in forebrain region indicated (dashed white rectangle on the left). 6 regions-of-interest (ROIs) are outlined. The red arrow marks cadaverine stimulus onset. White arrows indicate the locations and times of each ROIs near a calcium event's peak. Scale bars: 100 µm. **(f)** The corresponding calcium signal traces of 38 representative neurons recorded before and after the presentation of 1 mM cadaverine, with onset indicated by the red arrow and dotted red line. Scale bar: 10 seconds. **(g)** Summary of key differences between Fish-on-Chip 1.0 and 2.0. The enhanced 2.0 platform eliminates the need for tilting or right-eye ablation in larvae, allowing for naturalistic, whole-body and brain-wide behavioral-neural recordings during spontaneous behavior and chemosensory cue presentations.

Supplementary Figure 3

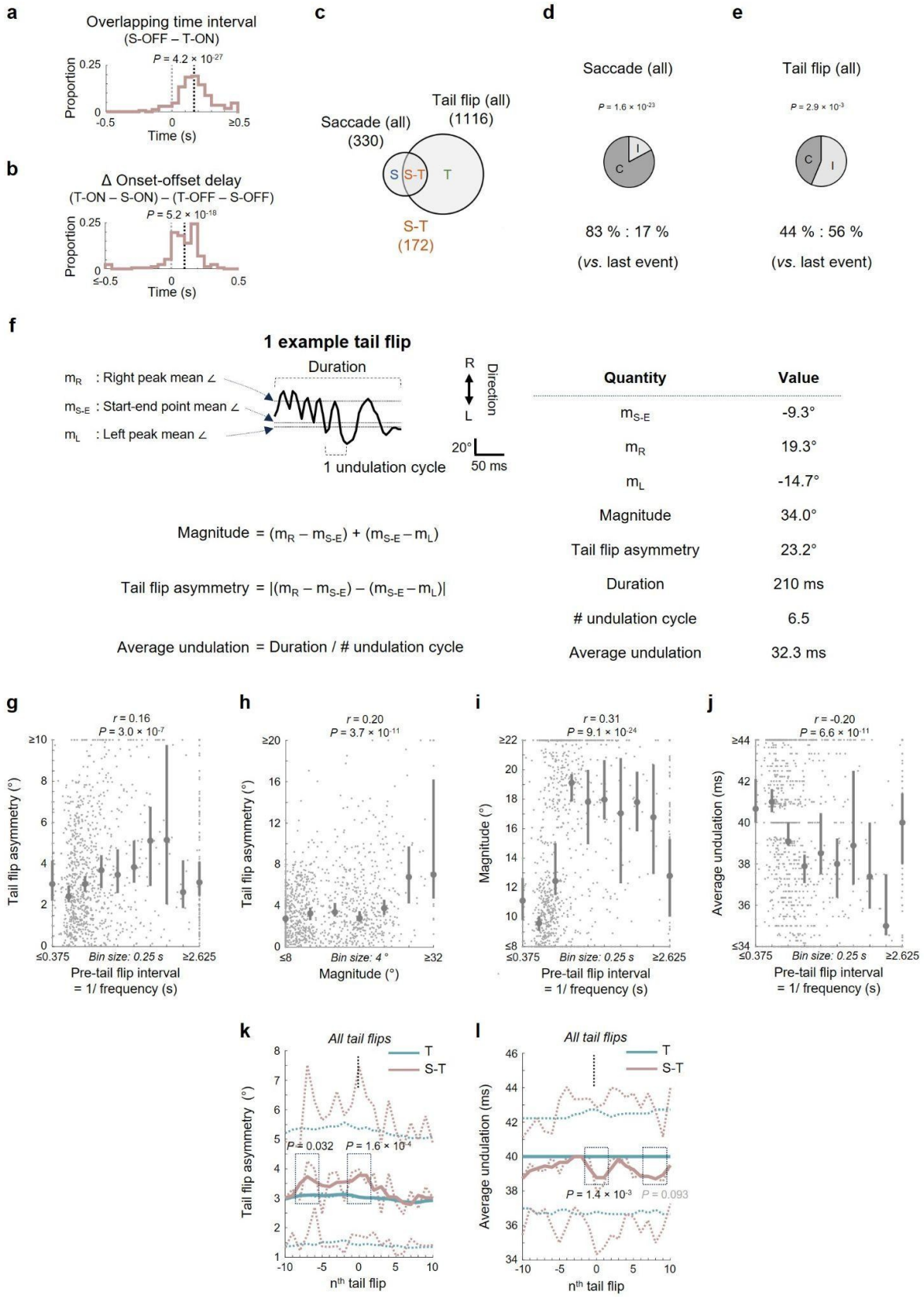

Supplementary Figure 3. Additional analysis of spontaneous saccade-tail flip coordination. (a) & **(b)** Histograms showing **(a)** overlapping time interval and **(b)** difference in onset-offset delay of coupled saccade-tail flip (S-T) events. Note that the precision of measurements for the onset and offset for saccade and tail flip were 0.0625s and 0.0025s due to the respective sampling rates. Black and gray dashed lines indicate median and zero respectively. *P*-values: Two-sided Wilcoxon signed-rank test. **(c)** Venn diagram showing all counts of spontaneous saccades, tail flips and S-T events (n = 5 larvae). **(d)** & **(e)** Pie charts showing the proportions of contra- and ipsilateral turns, comparing the directionality of **(d)** saccades and their preceding events, and **(e)** tail flips and their preceding events. *P*-values: Two-sided binomial test. **(f)** Illustration of the various kinematic parameters of an example tail flip. Dashed lines indicate the right peak mean angle, start-end point mean angle, and left peak mean angle. **(g)–(j)** Medians and 95% confidence intervals (based on bootstrapping with 1000 resamples) of all tail flips' **(g)** tail flip asymmetry vs. their pre-tail flip interval [1/ frequency] (binned), **(h)** tail flip asymmetry vs. their magnitude (binned), **(i)** magnitude vs. their pre-tail flip interval [1/ frequency] (binned) and **(j)** average undulation vs. their pre-tail flip interval [1/ frequency]. Gray dots are individual data points. Spearman's rank correlation coefficients (r) and associated *P*-values are shown. **(k)** Tail flip asymmetry of self and flanking tail flips for all S-T events or all independent tail flips (T) regardless of tail flip asymmetry. **(l)** Average undulation of self and flanking tail flips for all S-T or all T events regardless of tail flip asymmetry. In **(k)** & **(l)**, the thin curves represent the medians, 75th and 25th percentiles of all events. *P*-values: Two-sided Wilcoxon rank-sum test comparing peaks and ± 1 events.

Supplementary Figure 4

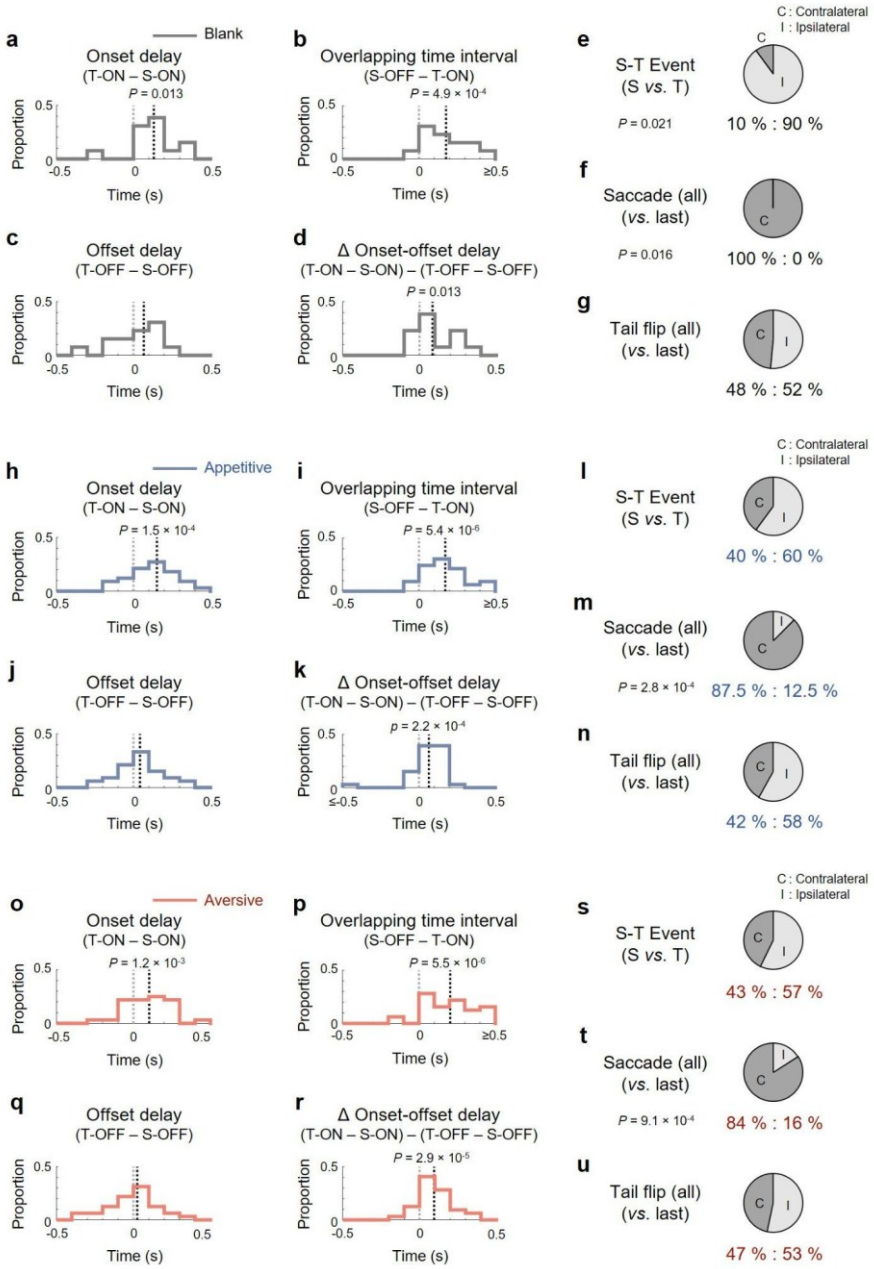

Supplementary Figure 4. Temporal and directional characteristics of coupled saccade-tail flip (S-T) events under chemical stimulus presentation. (a)–(d) Histograms of saccade-tail flip **(a)** onset delay, **(b)** overlapping time interval, **(c)** offset delay and **(d)** difference in onset-offset delay of S-T events during blank stimuli. Note that the precision of measurements for the onset and offset for saccade and tail flip were 0.0625s and 0.0025s due to the respective sampling rates. Black and gray dashed lines indicate median and zero respectively. *P*-values: Two-sided Wilcoxon signed-rank test. **(e)–(g)** Pie charts showing the proportions of contra- and ipsilateral turns, comparing the directionality of **(e)** saccades and turns in S-T events, **(f)** saccades and their preceding events, and **(g)** tail flips and their preceding events. *P*-values: Two-sided binomial test. **(h)–(n)** and **(o)–(u)** are similar to **(a)–(g)** but showing results during appetitive and aversive chemical presentations, respectively. Abbreviations: S, saccade; T, tail flip; ON, onset; OFF, offset.

Supplementary Figure 5

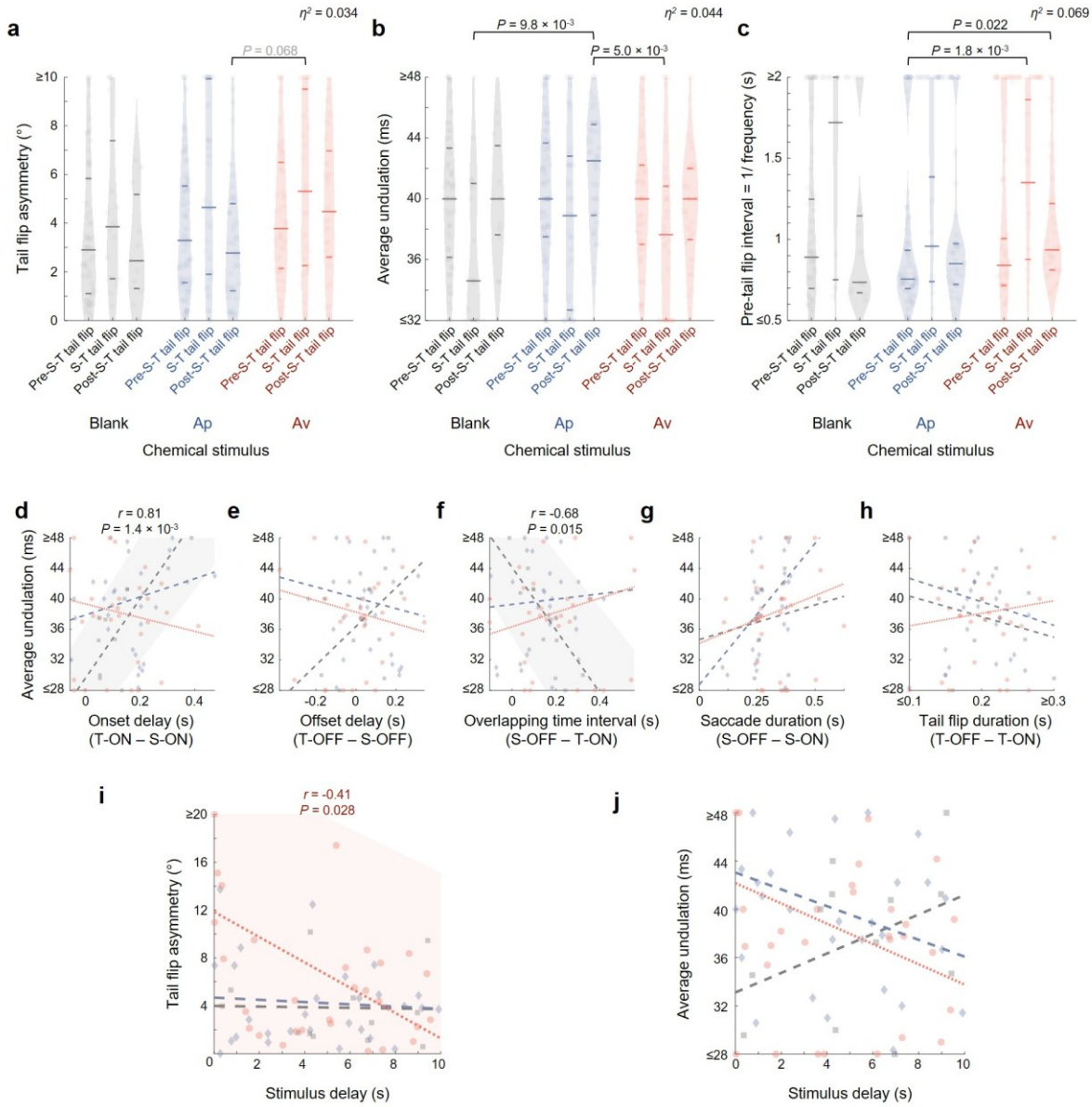

Supplementary Figure 5. Additional kinematic and temporal analysis of spontaneous coupled saccade-tail flip (S-T) coordination during chemical presentation. (a)–(c) Kinematic parameters of tail flips subgrouped into chemical stimulus-associated pre-S-T (independent), S-T and post-S-T (independent) tail flips including **(a)** tail flip asymmetry, **(b)** average undulation, and **(c)** pre-tail flip interval [1/ frequency]. Horizontal lines indicate the medians, 75th and 25th percentiles. Shadows of the violin plots scale according to the probability density function. *P*-values: Kruskal–Wallis test with Dunn-Sidak post hoc test. Eta squared (η^2) is provided as a measure of effect size. Abbreviations: Ap, appetitive; Av, aversive. **(d)–(h)** Scatter plots of average undulation vs. various temporal parameters for S-T events, including saccade-tail flip **(d)** onset delay, **(e)** offset delay, **(f)** overlapping time interval, **(g)** saccade duration, and **(h)** tail flip duration. **(i)** & **(j)** Scatter plots showing **(i)** tail flip asymmetry and **(j)** average undulation vs. stimulus delay for S-T events. In **(d)–(j)** Individual data points are shown in squares, diamonds and circles for the blank control, appetitive and aversive chemical groups respectively. Lines show best linear fits of each data group and shadows show 95% prediction confidence intervals of the blank control data group in **(d)** & **(f)** (the only that exhibited significant associations) and aversive chemical data group in **(i)** (the only that exhibited significant association). Pearson's correlation coefficient (r) and associated *P*-value are shown for the **(d)** & **(f)** blank control and **(i)** aversive chemical data points.

Supplementary Figure 6

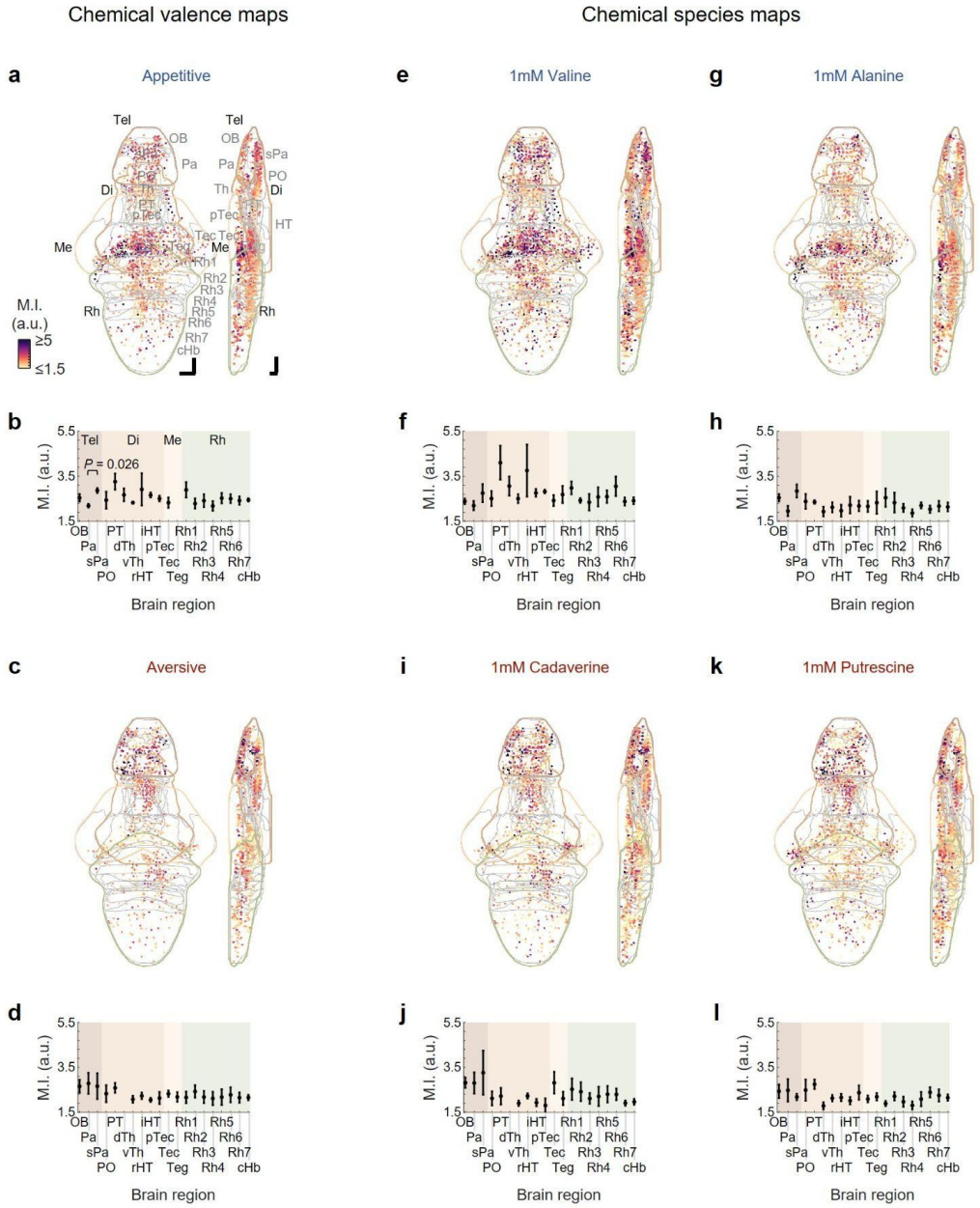

Supplementary Figure 6. Brain-wide chemical representation. (a) Mean intensity (to transverse and sagittal planes) of mean mutual information (M.I.) between the calcium signals of appetitive valence-encoding regions-of-interest (ROIs) and the appetitive stimulus regressors ((I_{valine} + $I_{alanine}$)/2, see **Methods**). **(b)** Regional mean ± S.E.M. (across larvae) of mean appetitive M.I. ((I_{valine} + $I_{alanine}$)/2). *P*-value: Two-sided *t*-test comparing the pallium and the subpallium. **(c)** & **(d)** Similar to **(a)** & **(b)** but for mean aversive chemical M.I. (($I_{cadaverine}$ + $I_{putrescine}$)/2) and aversive valence-encoding ROIs. **(e)** Mean intensity projections (to transverse and sagittal planes) of M.I. between the calcium signals of 1 mM valine-encoding ROIs and the stimulus regressor (I_{valine}, see **Methods**). **(f)** Regional mean ± S.E.M. (across larvae) of sensory M.I. **(g)**–**(l)** Similar to **(e)** & **(f)** but for **(g)** & **(h)** alanine ($I_{alanine}$), **(i)** & **(j)** cadaverine ($I_{cadaverine}$) and **(k)** & **(l)** putrescine ($I_{putrescine}$), all at 1 mM. The major brain regions (Tel: telencephalon, Di: diencephalon, Me: mesencephalon and Rh: rhombencephalon) are color-coded. Abbreviations of brain regions: Same as in **Figure 5d**. In all plots, data are pooled from n = 5 larvae. Scale bars: 50 µm in the Z-Brain Atlas space.

Supplementary Figure 7

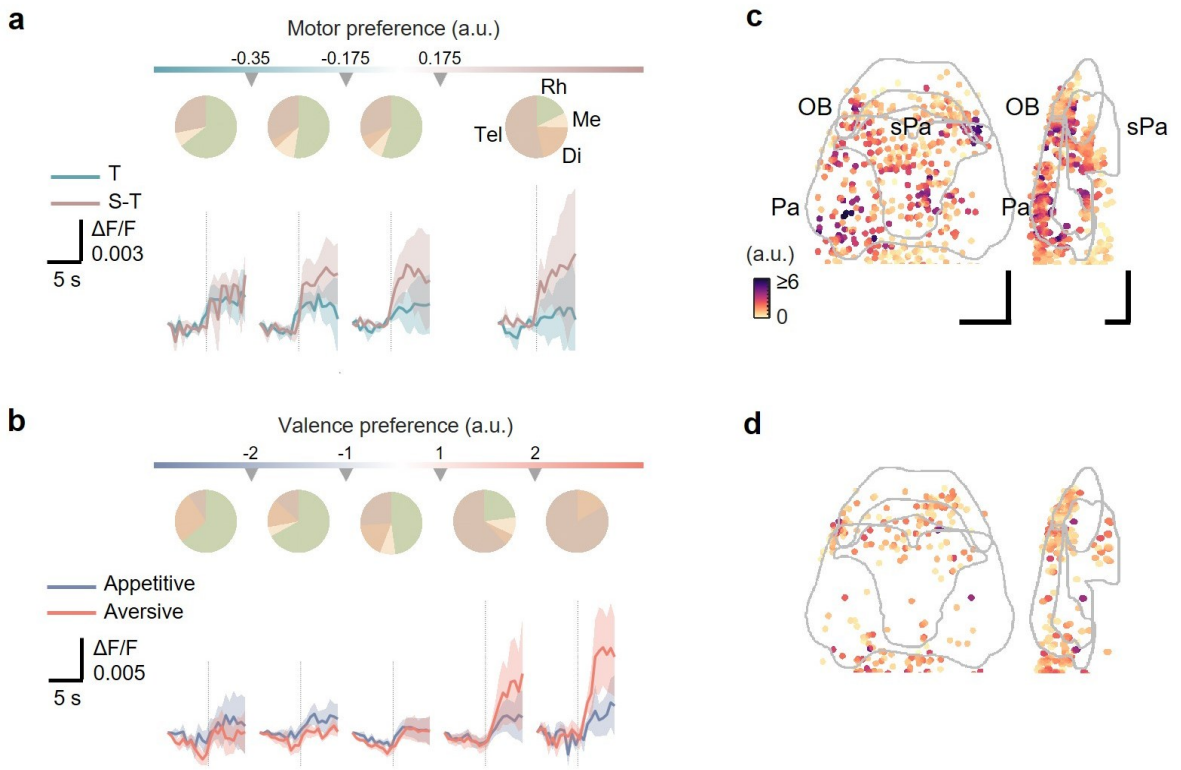

Supplementary Figure 7. Additional analysis on brain-wide valence and motor representations. (a) Upper panel: Pie charts showing the regional distributions of regions-of-interest (ROIs) (median proportions across larvae) with motor preference in different ranges. Lower panel: Mean ± S.E.M. (across larvae) responses of motor-encoding ROIs with motor preference in different ranges. Dotted vertical lines indicate the times of tail flip onsets (in a corresponding neuronal imaging frame). **(b)** Upper panel: Pie charts showing the regional distributions of ROIs (median proportions across larvae) with valence preference in different ranges. Lower panel: Mean ± S.E.M. (across larvae) responses of valence-encoding ROIs with valence preference in different ranges. Dotted vertical lines indicate the time points of stimulus onsets (between two neuronal imaging frames). In **(a)** and **(b)**, the major brain regions (Tel: telencephalon, Di: diencephalon, Me: mesencephalon and Rh: rhombencephalon) are color-coded. The neural activity data correspond to the behavioral data reported in **Figures 2** & **4**, collected from n = 5 larvae. **(c)** & **(d)** Zoom-in maps showing the forebrain regions olfactory bulb, pallium and subpallium ROIs preferring **(c)** S-T event and aversive valence in **Figure 5h**, and **(d)** independent tail flip and appetitive valence in **Figure 5j**. Scale bars: 50 µm in the Z-Brain Atlas space.

Supplementary Figure 8

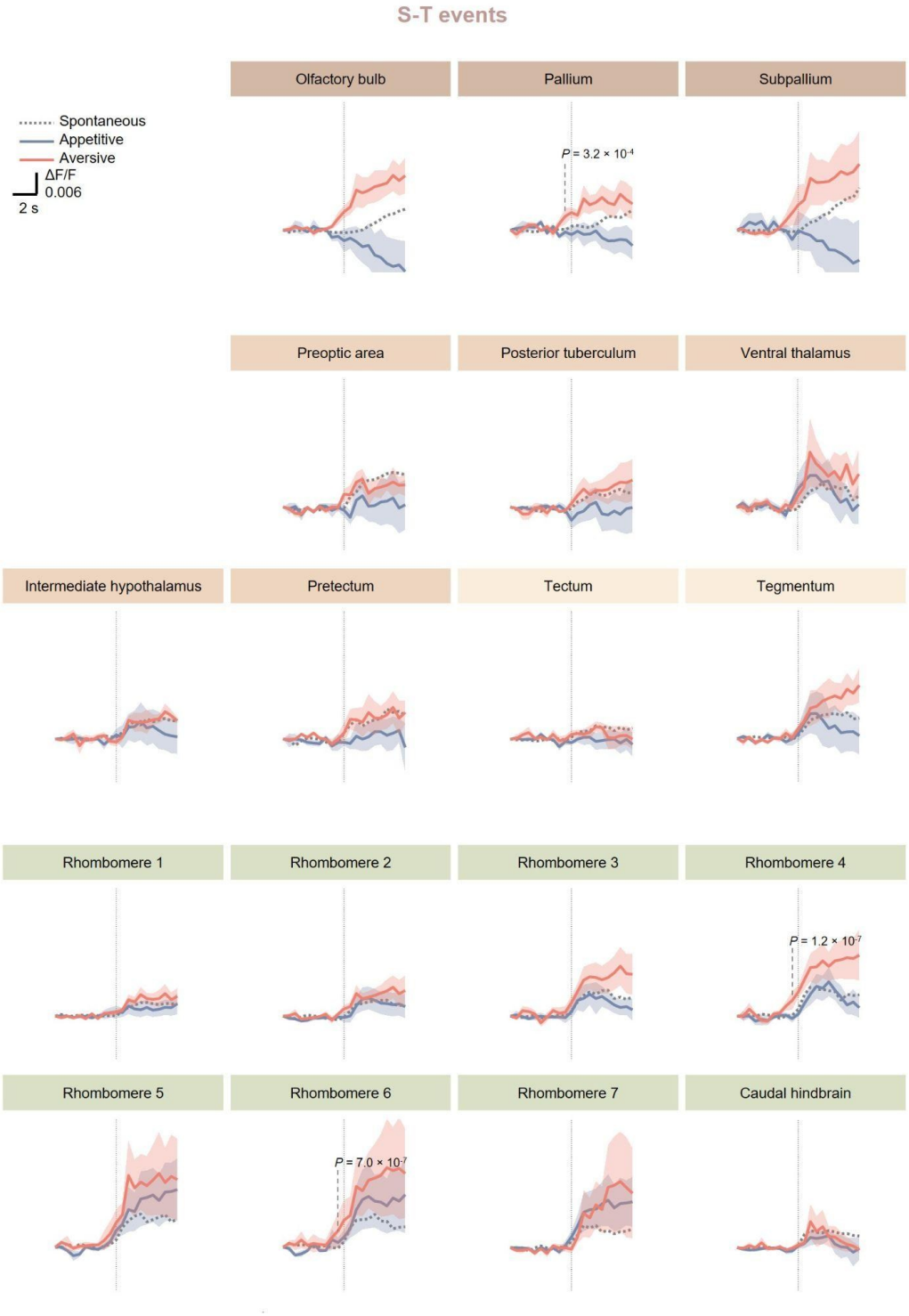

Supplementary Figure 8. Neuronal activity associated with chemosensory-driven coupled saccade-tail flip (S-T) events across different brain regions. Mean ± S.E.M. (across $n = 5$ larvae) responses of motor-encoding regions-of-interest (ROIs) in the different brain regions, aligned to the onset of chemosensory cue-associated S-T events. Dotted traces show the corresponding neuronal responses of spontaneous S-T events. Dotted vertical lines indicate tail flip onsets (in a corresponding neuronal imaging frame). *P*-values: Right-sided *Z*-tests comparing pre-chemical cue-associated event neuronal activity at each time point to zero. Significance was set at 2.5 standard deviations (S.D.), with S.D. estimated from spontaneous event baseline activity variability. Adjustment for multiple comparisons across time points and brain regions was made using the Benjamini-Hochberg procedure.

Supplementary Figure 9

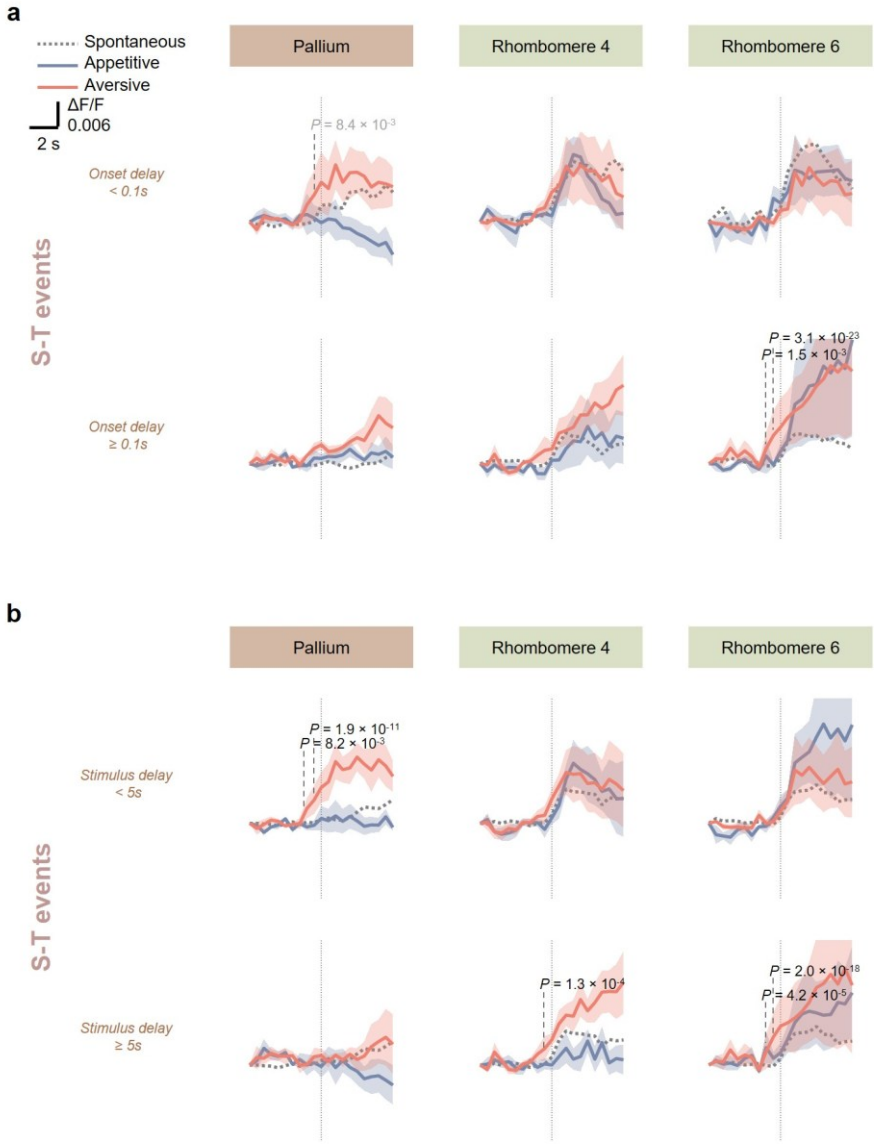

Supplementary Figure 9. Additional analysis on neural activity underlying chemosensory-driven coupled saccade-tail flip (S-T) events. Mean ± S.E.M. (across n = 5 larvae) responses of motor-encoding regions-of-interest (ROIs) in the pallium, rhombomere 4 and rhombomere 6, classified according to **(a)** saccade-tail flip onset delay [< 0.1 seconds (upper) or ≥ 0.1 seconds (lower)] and **(b)** stimulus-tail flip delay [< 5 seconds (upper) or ≥ 5 seconds (lower)], and aligned to the onset of chemosensory cue-associated S-T events. Dotted traces show the corresponding neuronal responses of spontaneous S-T events (note that in **(b)**, spontaneous S-T events were not classified according to stimulus-tail flip delay). Dotted vertical lines indicate tail flip onsets (in a corresponding neuronal imaging frame). P-values: Right-sided Z-tests comparing pre-chemical cue-associated event neuronal activity at each time point to zero. Significance was set at 2.5 standard deviations (S.D.), with S.D. estimated from spontaneous event baseline activity variability. Adjustment for multiple comparisons across time points and brain regions was made using the Benjamini-Hochberg procedure. Statistical significance: Black, significant; gray, near-significant.

Supplementary Figure 10

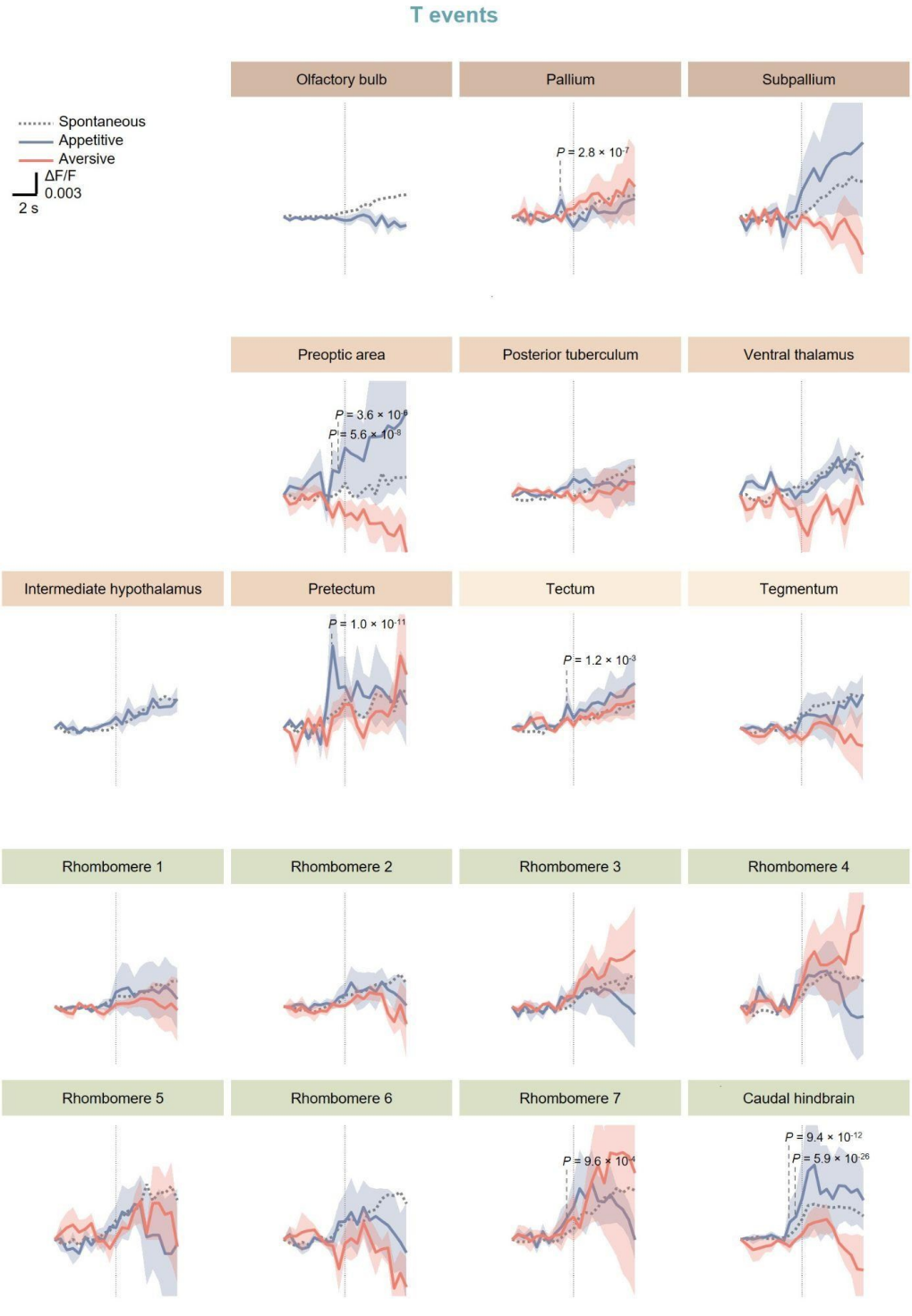

Supplementary Figure 10. Neuronal activity associated with chemosensory-driven independent tail flips (T events) across brain regions. Mean ± S.E.M. (across n = 5 larvae) responses of motor-encoding regions-of-interest (ROIs) in the different brain regions, aligned to the onset of independent tail flips during chemical cue presentation. Dotted traces show the corresponding neuronal responses of spontaneous independent tail flips. Dotted vertical lines indicate tail flip onsets (in a corresponding neuronal imaging frame). P-values: Right-sided Z-tests comparing pre-chemical cue-associated event neuronal activity at each time point to zero. Significance was set at 2.5 standard deviations (S.D.), with S.D. estimated from spontaneous event baseline activity variability. Adjustment for multiple comparisons across time points and brain regions was made using the Benjamini-Hochberg procedure.